

PHYSICS

High-Tech Materials Could Render Objects Invisible

No, this isn't the 1 April issue of *Science*, and yes, you read the headline correctly. Materials already being developed could funnel light and electromagnetic radiation around any object and render it invisible, theoretical physicists predict online in *Science* this week (www.sciencemag.org/cgi/content/abstract/1125907 and ... 1126493). In the near future, such cloaking devices might shield sensitive equipment from disruptive radio waves or electric and magnetic fields. Cloaks that hide objects from prying eyes might not be much further off, researchers say.

The papers are "visionary," says George Eleftheriades, an electrical engineer at the University of Toronto in Canada. "It's pioneering work that sets the stage for future research." Greg Gbur, a theoretical physicist at the University of North Carolina, Charlotte, notes that others have studied invisibility but says the new papers describe more precisely how to achieve it. "Each gives specific examples of how you might design an invisibility device," he says.

From spaceships that vanish in *Star Trek* movies to Harry Potter hiding beneath his imperceptible cloak, invisibility has been a mainstay of science fiction and fantasy. But it might become a reality thanks to emerging "metamaterials," assemblages of tiny rods, c-shaped metallic rings, etc., that respond to electromagnetic fields in new and highly controllable ways. John Pendry of Imperial College London and colleagues, and Ulf Leonhardt of the University of St. Andrews, U.K., independently calculated how the properties of a shell metamaterial must be tailored to usher light around an object inside it. An observer would see whatever is behind the object as if the thing weren't there, Leonhardt says.

The theorists exploit the fact that light is always in a hurry, taking the quickest route between two points. That's not always a straight line, because light travels at different speeds in different materials, and it opts for the path that minimizes the total time of transit. So when light passes from, say, air into glass, its path may bend, which is why ordinary lenses focus light.

Pendry and colleagues and Leonhardt calculated how the speed of light would have to vary from point to point within a spherical or cylindrical shell to make the light flow around the hole in the middle. Light must travel faster



No see? Forget the Invisible Man's transparency potion; new materials might ferry light around an object, making it invisible.

toward the inner surface of the shell. In fact, along the inner surface, light must travel infinitely fast. That doesn't violate Einstein's theory of relativity because within a material, light has two speeds: the one at which the ripples in a wave of a given frequency zip along, and the one at which energy and information flow. Only the second must remain slower than light in a vacuum, as it does in a metamaterial.

U.S. COURTS

'Disappointed' Butler Exhausts Appeals

Thomas Butler's legal journey has come to an end. On 15 May, the U.S. Supreme Court declined to take up the case of the physician and microbiologist who received a 2-year prison sentence for shipping plague samples to Tanzania without the required permits and for defrauding his employer, Texas Tech University in Lubbock (*Science*, 19 December 2003, p. 2054).

Butler declined to be interviewed, but his wife Elizabeth says her husband is "very disappointed." Butler is working in Lubbock at a job unrelated to his professional training, she says, and weighing offers to rebuild his career. "This has been a tremendous blow," she adds, "but we are healing little by little."

In January 2003, Butler reported vials containing the plague bacterium *Yersinia pestis* missing from his lab; after questioning by the FBI, he signed a statement, which he later withdrew, saying he had accidentally destroyed the samples. In his trial, the jury dismissed all but one of the government's charges relating to illegal shipping and handling of plague samples but found Butler guilty of

The invisibility isn't perfect: It works only in a narrow range of wavelengths.

The authors map out the necessary speed variations and leave it to others to design the materials that will produce them. But researchers already know how to design metamaterials to achieve such bizarre properties, at least for radio waves, says Nader Engheta, an electrical engineer at the University of Pennsylvania. "It's not necessarily easy, but the recipes are there," says Engheta, who last year proposed using a metamaterial coating to counteract an object's ability to redirect light, making combination nearly transparent.

Cloaking devices for radio waves could appear within 5 years, Gbur says, and cloaks for visible light are conceivable. Pendry notes that even a cloak for static fields would, for example, let technicians insert sensitive electronic equipment into a magnetic resonance imaging machine without disturbing the machine's precisely tuned magnetic field.

Alas, even if invisibility proves possible, it may not work the way it does in the movies. For example, a cloaking device would be useless for spying, Pendry says. "Nobody can see you in there, but of course you can't see them, either." Keeping track of your always-invisible device might be a pain, too.

—ADRIAN CHO

fraud involving fees for clinical trials he had conducted at Texas Tech. Last fall, a three-judge panel on the U.S. Court of Appeals for the Fifth Circuit upheld his conviction (*Science*, 4 November 2005, p. 758); the full appeals court declined to review the case.

"I have never in my career seen someone who was handed such a gross injustice," says his attorney, George Washington University law professor Jonathan Turley. Turley says that the fraud charges, which the government added after Butler refused to accept a plea bargain, concerned a dispute between the researcher and his employer that would not otherwise have been prosecuted criminally.

Butler, 64, was transferred to a halfway house in November after having served 19 months of his sentence and came home in late December. His supporters, including chemistry Nobel laureate Peter Agre of Duke University in Durham, North Carolina, are hoping against hope for a presidential pardon, if not from George W. Bush then possibly from his successor.

—MARTIN ENSERINK

than in the rest of the disk. The correlation remains notable even if we do not apply a thickness filter to the data or if we use another definition of the thickness (3, 11). The two maps are not independent, however; changing the density distribution in the arms will necessarily produce changes in the measured thickness unless the perturbations are distributed in the same way as the initial distribution. The alignment of overdensities with regions of reduced thickness was suggested previously (3). This alignment has not been observed in other galaxies because surface density maps are most easily made for face-on galaxies where there is no information about the thickness of the gas layer.

The radial profile of the HI disk has been a matter of controversy for many years. A sharp falloff in HI emission as a function of velocity has long been known (18), but this need not correspond to an abrupt radial cutoff in the disk density (19). Velocity dispersion will cause features to be smeared along the line of sight by confusing the velocity-distance transformation, resulting in the radially elongated features near the edges of maps (Fig. 3). The radial extent of the spiral arms provides a minimum cutoff radius for the Galactic gas disk; in other words, it is not possible for the gas to have spiral structure beyond where the HI disk ends. This radius is only a lower limit, because it is possible that there is gas beyond where the spiral structure ends that does not participate in the spiral structure or that past some radius the arms are too weak to be detected by the unsharp masking. Near 25-kpc Galactocentric radius, both the surface density and the thickness perturbation maps (Fig. 3) change from spiral patterns to features elongated along the line of sight. This is most clearly seen in the south; the transition radius is not immediately obvious in the north. Thus, the HI gas disk must extend to at least 25 kpc from the Galactic center in the south, about three times the Sun-Galactic center distance. A related conclusion is that gas within the cutoff radius is kinematically settled into a disk; otherwise it would be unlikely to respond to the spiral density waves.

It is useful to fit four-armed models to our density perturbation map. We used logarithmic spiral arms that start at the Solar circle:

$$\log(R/R_0) = [\phi(R) - \phi_0] \tan \psi \quad (2)$$

where ψ is the pitch angle and ϕ_0 is the Galactocentric azimuth at the Solar circle. Our fitting method was designed to trace the regions of gas overdensity. For each of the four arms apparent in Fig. 1, we investigated an evenly spaced grid of these two free parameters for ranges of values that connect the overdense contours. For each combination of ψ and ϕ_0 , we linearly interpolated the value of Π for the locus of points along each arm. Any points that fall in the excluded regions were ignored. We used the median of the list of interpolated

values as a measure of the goodness of fit for each curve. In this scheme, arms with values of ψ and ϕ_0 that trace overdense regions will naturally have a large median and thus a large goodness of fit. The best fit values of ψ and ϕ_0 for each of the four arms are given (Table 1). Other fits that connect a different set of features in the map could be drawn, because assigning a unique arm pattern to a map is not possible. We find pitch angles for the outer arms in the range from 20° to 25°; this is larger than the value of $\psi \approx 13^\circ$ averaged over a variety of tracers (20). This does not necessarily imply a disagreement, however, because the arms could be unwinding in their outer regions.

Various models of the locations of the arms have been proposed. We compared our map to a model derived from regions of ionized hydrogen (21–23); the model consists of two pairs of mirror symmetric arms following logarithmic spirals. We denoted this as the symmetric model (Fig. 4). The symmetric model fits Π reasonably well over much of the southern sky; the agreement is poor in the north where the spiral structure is less prominent, possibly because of the larger thickness of the northern gas (11). Gas that is dynamically warmer is less likely to respond to spiral density waves, and the azimuthally averaged thickness of the northern gas is nearly twice that of the southern gas at $R = 20$ kpc.

There are several places where the symmetric model deviates from the data. For example, the arm in the north ($R \approx 13$ kpc) falls in between two of the model's arms; forcing the arms to be mirror-imaged pairs is too strong a restriction. Features near the excluded regions could result from a large-scale ordered velocity structure that has not been included in our rotation model. Elliptical streamlines with $m = 2$ could cause such an effect (11). Images of other galaxies suggest that the spiral arms may bifurcate into spurs in the outer disk. The

structure of the Perseus and Carina arms past $R \approx 20$ kpc is suggestive of this behavior.

References and Notes

1. H. C. van de Hulst, C. A. Muller, J. H. Oort, *Bull. Astron. Inst. Neth.* **12**, 117 (1954).
2. F. Kerr, G. Westerhout, in *Galactic Structure*, vol. 5 of *Stars and Stellar Systems*, A. Blaauw, M. Schmidt, Eds. (Univ. Chicago Press, Chicago, IL, 1965), pp. 167–202.
3. A. P. Henderson, P. D. Jackson, F. J. Kerr, *Astrophys. J.* **263**, 116 (1982).
4. D. Malin, *Am. Astron. Soc. Photo Bull.* **16**, 10 (1977).
5. P. M. W. Kalberla et al., *Astron. Astrophys.* **440**, 775 (2005).
6. D. Hartmann, W. B. Burton, *Atlas of Galactic Neutral Hydrogen* (Cambridge Univ. Press, Cambridge, 1997).
7. E. Bajaja et al., *Astron. Astrophys.* **440**, 767 (2005).
8. E. M. Arnal, E. Bajaja, J. J. Larrarte, R. Morras, W. G. L. Pöppel, *Astron. Astrophys. Suppl. Ser.* **142**, 35 (2000).
9. M. J. Reid, *Annu. Rev. Astron. Astrophys.* **31**, 345 (1993).
10. R. P. Olling, M. R. Merrifield, *Mon. Not. R. Astron. Soc.* **297**, 943 (1998).
11. E. S. Levine, L. Blitz, C. Heiles, *Astrophys. J.* **643**, 881 (2006).
12. N. M. McClure-Griffiths, J. M. Dickey, B. M. Gaensler, A. J. Green, *Astrophys. J.* **607**, L127 (2004).
13. J. S. Miller, *Astrophys. J.* **151**, 473 (1968).
14. Y. Xu, M. J. Reid, X. W. Zheng, K. M. Menten, *Science* **311**, 54 (2006); published online 7 December 2005 (10.1126/science.1120914).
15. W. B. Burton, *Astron. Astrophys.* **10**, 76 (1971).
16. M. A. Tuve, S. Lundsager, *Astron. J.* **77**, 652 (1972).
17. C. Yuan, *Astrophys. J.* **158**, 871 (1969).
18. N. H. Dieter, *Astron. Astrophys.* **12**, 59 (1971).
19. G. R. Knapp, S. D. Tremaine, J. E. Gunn, *Astron. J.* **83**, 1585 (1978).
20. J. P. Vallée, *Astron. J.* **130**, 569 (2005).
21. W. W. Morgan, A. E. Whitford, A. D. Code, *Astrophys. J.* **118**, 318 (1953).
22. Y. M. Georgelin, Y. P. Georgelin, *Astron. Astrophys.* **49**, 57 (1976).
23. R. J. Wainscoat, M. Cohen, K. Volk, H. J. Walker, D. E. Schwartz, *Astrophys. J. Suppl. Ser.* **83**, 111 (1992).
24. We thank P. Kalberla for providing a copy of the LAB HI survey and J. Peek, C. Laver, and T. Robshaw for helpful advice regarding plots. E.S.L. and L.B. were supported by NSF grant AST 02-28963. C.H. was supported by NSF grant AST 04-06987.

7 April 2006; accepted 22 May 2006

Published online 1 June 2006;

10.1126/science.1128455

Include this information when citing this paper.

Optical Conformal Mapping

Ulf Leonhardt

An invisibility device should guide light around an object as if nothing were there, regardless of where the light comes from. Ideal invisibility devices are impossible, owing to the wave nature of light. This study develops a general recipe for the design of media that create perfect invisibility within the accuracy of geometrical optics. The imperfections of invisibility can be made arbitrarily small to hide objects that are much larger than the wavelength. With the use of modern metamaterials, practical demonstrations of such devices may be possible. The method developed here can also be applied to escape detection by other electromagnetic waves or sound.

According to Fermat's principle (1), light rays take the shortest optical paths in dielectric media, where the refractive index n integrated along the ray trajectory defines the path length. When n is spatially varying, the shortest optical paths are not straight lines, but are

curved. This light bending is the cause of many optical illusions. Imagine a situation where a medium guides light around a hole in it. Suppose that all parallel bundles of incident rays are bent around the hole and recombined in precisely the same direction as they entered the medium. An

observer would not see the difference between light passing through the medium or propagating across empty space (or, equivalently, in a uniform medium). Any object placed in the hole would be hidden from sight. The medium would create the ultimate optical illusion: invisibility (2).

However, it has been proved (3, 4) that perfect invisibility is unachievable, except in a finite set of discrete directions where the object appears to be squashed to infinite thinness and for certain objects that are small as compared with the wavelength (5, 6). In order to carry images, though, light should propagate with a continuous range of spatial Fourier components, i.e., in a range of directions. The mathematical reason for the impossibility of perfect invisibility is the uniqueness of the inverse-scattering problem for waves (3): the scattering data, i.e., the directions and amplitudes of the transmitted plane-wave components determine the spatial profile of the refractive index (3). Therefore, the scattering data of light in empty space are only consistent with the propagation through empty space. Perfect illusions are thus thought to be impossible due to the wave nature of light.

On the other hand, the theorem (3) does not limit the imperfections of invisibility—they may be very small—nor does it apply to light rays, i.e., to light propagation within the regime of geometrical optics (1). This study develops a general recipe for the design of media that create perfect invisibility for light rays over a continuous range of directions. Because this method is based on geometrical optics (1), the inevitable imperfections of invisibility can be made exponentially small for objects that are much larger than the wavelength of light.

To manufacture a dielectric invisibility device, media are needed that possess a wide range of the refractive index in the spectral domain where the device should operate. In particular, Fermat's Principle (1) seems to imply that $n < 1$ in some spatial regions, because only in this case the shortest optical paths may go around the object without causing phase distortions. In our example, n varies from 0 to about 36. In practice, one could probably accept a certain degree of visibility that substantially reduces the demands on the range of the refractive index.

Extreme values of n occur when the material is close to resonance with the electromagnetic field. Metamaterials (7) with man-made resonances can be manufactured with appropriately designed circuit boards, similar to the ones used for demonstrating negative refraction (8). The quest for the perfect lens (9) has led to recent improvements (7, 10–13) mainly focused on tuning the magnetic susceptibilities. In such metamaterials, each individual circuit plays the role of an artificial atom with tunable resonances. With these artificial dielectrics, invisibility could be reached for fre-

quencies in the microwave-to-terahertz range. In contrast, stealth technology is designed to make objects of military interest as black as possible to radar where, using impedance matching (14), electromagnetic waves are absorbed without reflection, i.e., without any echo detectable by radar. Recently, nanofabricated metamaterials with custom-made plasmon resonances have been demonstrated (13) that operate in the visible range of the spectrum and may be modified to reach invisibility.

The method used here is general and also applicable to other forms of wave propagation—for example, to sound waves, where the index n describes the ratio of the local phase velocity of the wave to the bulk value, or to quantum-mechanical matter waves, where external potentials act like refractive-index profiles (1). For instance, one could use the profiles of n described here to protect an enclosed space from any form of sonic tomography. This study examines the simplest nontrivial case of invisibility, an effectively two-dimensional situation, by applying conformal mapping (15) to solve the problem—an elegant technique used in research areas as diverse as electrostatics (14), fluid mechanics (16), classical mechanics (17–20), and quantum chaos (21, 22).

Consider an idealized situation: a dielectric medium that is uniform in one direction and light of wave number k that propagates orthogonal to that direction. In practice, the medium will have a finite extension and the propagation direction of light may be slightly tilted without causing an appreciable difference to the ideal case. The medium is characterized by the refractive-index profile $n(x, y)$. To satisfy the validity condition of geometrical optics, $n(x, y)$ must not vary by much over the scale of an optical wavelength $2\pi/k$ (1). To describe the spatial coordinates in the propagation plane, complex numbers $z = x + iy$ are used with the partial derivatives $\partial_x = \partial_z + \partial_z^*$ and $\partial_y = i\partial_z - i\partial_z^*$, where the asterisk symbolizes complex conjugation. In the case of a gradually varying refractive-index profile, both amplitudes ψ of the two polarizations of light obey the Helmholtz equation (1)

$$(4\partial_z^*\partial_z + n^2k^2)\psi = 0 \quad (1)$$

written here in complex notation with the Laplace operator $\partial_x^2 + \partial_y^2 = 4\partial_z^*\partial_z$. Suppose we introduce new coordinates w described by an analytic function $w(z)$ that does not depend on z^* . Such functions define conformal maps (15) that preserve the angles between the coordinate lines. Because $\partial_z^*\partial_z = |dw/dz|^2\partial_w^*\partial_w$, we obtain in w space a Helmholtz equation with the transformed refractive-index profile n' that is related to the original one as

$$n = n' \left| \frac{dw}{dz} \right| \quad (2)$$

Suppose that the medium is designed such that $n(z)$ is the modulus of an analytic function $g(z)$.

The integral of $g(z)$ defines a map $w(z)$ to new coordinates where, according to Eq. 2, the transformed index n' is unity. Consequently, in w coordinates, the wave propagation is indistinguishable from empty space where light rays propagate along straight lines. The medium performs an optical conformal mapping to empty space. If $w(z)$ approaches z for $w \rightarrow \infty$, all incident waves appear at infinity as if they have traveled through empty space, regardless

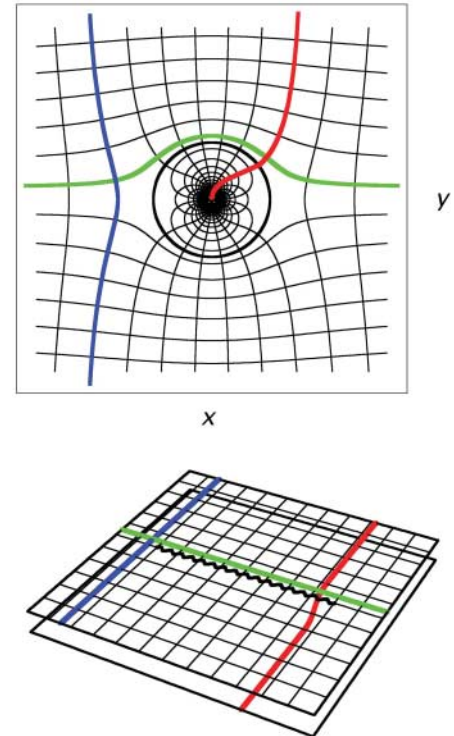


Fig. 1. Optical conformal map. A dielectric medium conformally maps physical space described by the points $z = x + iy$ of the complex plane onto Riemann sheets if the refractive-index profile is $|dw/dz|$ with some analytic function $w(z)$. The figure illustrates the simple map (3) where the exterior of a circle in the picture above is transformed into the upper sheet in the lower picture, and the interior of the circle is mapped onto the lower sheet. The curved coordinate grid of the upper picture is the inverse map $z(w)$ of the w coordinates, approaching a straight rectangular grid at infinity. As a feature of conformal maps, the right angles between the coordinate lines are preserved. The circle line in the figure above corresponds to the branch cut between the sheets below indicated by the curly black line. The figure also illustrates the typical fates of light rays in such media. On the w sheets, rays propagate along straight lines. The rays shown in blue and green avoid the branch cut and hence the interior of the device. The ray shown in red crosses the cut and passes onto the lower sheet where it approaches ∞ . However, this ∞ corresponds to a singularity of the refractive index and not to the ∞ of physical space. Rays like this one would be absorbed, unless they are guided back to the exterior sheet.

School of Physics and Astronomy, University of St Andrews, North Haugh, St Andrews KY16 9SS, Scotland. E-mail: ulf@st-andrews.ac.uk

of what has happened in the medium. However, as a consequence of the Riemann Mapping Theorem (15), nontrivial w coordinates occupy Riemann sheets with several ∞ , one on each sheet. Consider, for example, the simple map

$$w = z + \frac{a^2}{z}, \quad z = \frac{1}{2} \left(w \pm \sqrt{w^2 - 4a^2} \right) \quad (3)$$

illustrated in Fig. 1, that is realized by the refractive-index profile $n = |1 - a^2/z^2|$. The constant a characterizes the spatial extension of the medium. The function (3) maps the exterior of a circle of radius a on the z plane onto one Riemann sheet and the interior onto another. Light rays traveling on the exterior w sheet may have the misfortune of passing the branch cut between the two branch points $\pm 2a$. In continuing their propagation, the rays approach ∞ on the interior w sheet. Seen on the physical z plane, they cross the circle of radius a and approach the singularity of the refractive index at the origin. For general $w(z)$, only one ∞ on the Riemann structure in w space corresponds to the true ∞ of physical z space and the others to singularities of $w(z)$. Instead of traversing space, light rays may cross the branch cut to another Riemann sheet where

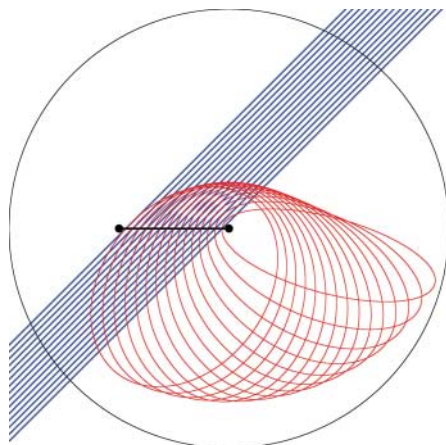


Fig. 2. Light guiding. The device guides light that has entered its interior layer back to the exterior, represented here using two Riemann sheets that correspond to the two layers, seen from above. Light on the exterior sheet is shown in blue and light in the interior, in red. At the branch cut, the thick line between the two points in the figure (the branch points), light passes from the exterior to the interior sheet. Here light is refracted according to Snell's law. On the lower sheet, the refractive-index profile (5) guides the rays to the exterior sheet in elliptic orbits with one branch point as focal point. Finally, the rays are refracted back to their original directions and leave on the exterior sheet as if nothing has happened. The circle in the figure indicates the maximal elongations of the ellipses. This circle limits the region in the interior of the device that light does not enter. The outside of the circle corresponds to the inside of the device. Anything beyond this circle is invisible.

they approach ∞ . Seen in physical space, the rays are irresistibly attracted toward some singularities of the refractive index. Instead of becoming invisible, the medium casts a shadow that is as wide as the apparent size of the branch cut. Nevertheless, the optics on Riemann sheets turns out to serve as a powerful theoretical tool for developing the design of dielectric invisibility devices.

All we need to achieve is to guide light back from the interior to the exterior sheet, i.e., seen in physical space, from the exterior to the interior layer of the device. To find the required refractive-index profile, we interpret the Helmholtz equation in w space as the Schrödinger equation (1) of a quantum particle of effective mass k^2 moving in the potential U with energy E such that $U - E = -n^2/2$ (1). We wish to send all rays that have passed through the branch cut onto the interior sheet back to the cut at precisely the same location and in the same direction in which they entered. This implies that we need a potential for which all trajectories are closed. Assuming

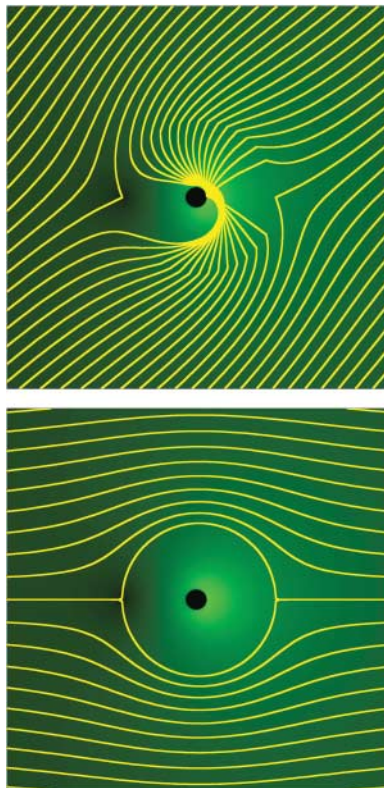


Fig. 3. Ray propagation in the dielectric invisibility device. The light rays are shown in yellow. The brightness of the green background indicates the refractive-index profile taken from the simple map (3) and the Kepler profile (5) with $r_0 = 8a$ in the interior layer of the device. The invisible region is shown in black. The upper panel illustrates how light is refracted at the boundary between the two layers and guided around the invisible region, where it leaves the device as if nothing were there. In the lower panel, light simply flows around the interior layer.

radial symmetry for $U(w)$ around one branch point w_1 , say $+2a$ in our example, only two potentials have this property: the harmonic oscillator and the Kepler potential (17). In both cases the trajectories are ellipses (17) that are related to each other by a transmutation of force according to the Amol'd-Kasner theorem (18–20). The harmonic oscillator corresponds to a Luneburg lens (23) on the Riemann sheet with the transformed refractive-index profile

$$n^2 = 1 - \frac{|w - w_1|^2}{r_0^2} \quad (4)$$

where r_0 is a constant radius. The Kepler potential with negative energy E corresponds to an Eaton lens (23) with the profile

$$n^2 = \frac{r_0}{|w - w_1|} - 1 \quad (5)$$

Note that the singularity of the Kepler profile in w space is compensated by the zero of $|dw/dz|$ at a branch point in physical space such that the total refractive index (2) is never singular. In both cases (4) and (5), r_0 defines the radius of the circle on the interior w sheet beyond which n'^2 would be negative and hence inaccessible to light propagation. This circle should be large enough to cover the branch cut. The inverse map $z(w)$ turns the outside of the circle into the inside of a region bounded by the image $z(w)$ of the circle line in w space. No light can enter this region. Everything inside is invisible.

Yet there is one more complication: Light is refracted (1) at the boundary between the exterior and the interior layer. Seen in w space, light rays encounter here a transition from the refractive index 1 to n' . Fortunately, refraction is reversible. After the cycles on the interior sheets, light rays are refracted back to their original directions (Fig. 2). The invisibility is not affected, unless the rays are totally reflected. According to Snell's Law (1), rays with angles of incidence θ with respect to the branch cut enter the lower sheet with angles θ' such that $n' \sin \theta' = \sin \theta$. If $n' < 1$, this equation may not have real solutions for θ larger than a critical angle Θ . Instead of entering the interior layer of the device, the light is totally reflected (1). The angle Θ defines the acceptance angle of the dielectric invisibility device, because beyond Θ , the device appears silvery instead of invisible. The transformed refractive-index profiles (4) and (5) at the boundary between the layers are lowest at the other branch point w_2 that limits the branch cut, $w_2 = -2a$, in our example. In the case of the harmonic-oscillator profile (4), n' lies always below 1, and we obtain the acceptance angle

$$\Theta = \arccos \left(\frac{|w_2 - w_1|}{r_0} \right) \quad (6)$$

For all-round invisibility, the radius r_0 should approach infinity, which implies that the entire

interior sheet is used for guiding the light back to the exterior layer. Fortunately, the Kepler profile (5) does not lead to total reflection if $r_0 \geq 2|w_2 - w_1|$. In this case, the invisible area is largest for

$$r_0 = 2|w_2 - w_1| \quad (7)$$

Figure 3 illustrates the light propagation in a dielectric invisibility device based on the simple map (3) and the Kepler profile (5) with $r_0 = 8a$. Here n ranges from 0 to about 36, but this example is probably not the optimal choice. One can choose from infinitely many conformal maps $w(z)$ that possess the required properties for achieving invisibility: $w(z) \sim z$ for $z \rightarrow \infty$ and two branch points w_1 and w_2 . The invisible region may be deformed to any simply connected domain by a conformal map that is the numerical solution of a Riemann-Hilbert problem (16). We can also relax the tacit assumption that w_1 connects the exterior to only one interior sheet, but to m sheets where light rays return after m cycles. If we construct $w(z)$ as $af(z/a)$ with some analytic function $f(z)$ of the required properties and a constant length scale a , the refractive-index profile $|dw/dz|$ is identical for all scales a . Finding the most practical design is an engineering problem that depends

on practical demands. This problem may also inspire further mathematical research on conformal maps in order to find the optimal design and to extend our approach to three dimensions.

Finally, we ask why our scheme does not violate the mathematical theorem (3) that perfect invisibility is unattainable. The answer is that waves are not only refracted at the boundary between the exterior and the interior layer, but also are reflected, and that the device causes a time delay. However, the reflection can be substantially reduced by making the transition between the layers gradual over a length scale much larger than the wavelength $2\pi/k$ or by using anti-reflection coatings. In this way, the imperfections of invisibility can be made as small as the accuracy limit of geometrical optics (1), i.e., exponentially small. One can never completely hide from waves, but can from rays.

References and Notes

- M. Born, E. Wolf, *Principles of Optics* (Cambridge Univ. Press, Cambridge, 1999).
- G. Gbur, *Prog. Opt.* **45**, 273 (2003).
- A. I. Nachman, *Ann. Math.* **128**, 531 (1988).
- E. Wolf, T. Habashy, *J. Mod. Opt.* **40**, 785 (1993).
- M. Kerker, *J. Opt. Soc. Am.* **65**, 376 (1975).
- A. Alu, N. Engheta, *Phys. Rev. E* **72**, 016623 (2005).
- D. R. Smith, J. B. Pendry, M. C. K. Wiltshire, *Science* **305**, 788 (2004).

- R. A. Shelby, D. R. Smith, S. Schultz, *Science* **292**, 77 (2001).
- J. B. Pendry, *Phys. Rev. Lett.* **85**, 3966 (2000).
- A. Grbic, G. V. Eleftheriades, *Phys. Rev. Lett.* **92**, 117403 (2004).
- T. J. Yen *et al.*, *Science* **303**, 1494 (2004).
- S. Linden *et al.*, *Science* **306**, 1351 (2004).
- A. N. Grigorenko *et al.*, *Nature* **438**, 335 (2005).
- J. D. Jackson, *Classical Electrodynamics* (Wiley, New York, 1998).
- Z. Nehari, *Conformal Mapping* (McGraw-Hill, New York, 1952).
- M. J. Ablowitz, A. S. Fokas, *Complex Variables* (Cambridge Univ. Press, Cambridge, 1997).
- L. D. Landau, E. M. Lifshitz, *Mechanics* (Pergamon, Oxford, 1976).
- V. I. Arnol'd, *Huygens & Barrow, Newton & Hooke* (Birkhäuser Verlag, Basel, 1990).
- T. Needham, *Am. Math. Mon.* **100**, 119 (1993).
- T. Needham, *Visual Complex Analysis* (Clarendon, Oxford, 2002).
- M. Robnik, *J. Phys. A* **16**, 3971 (1983).
- M. Robnik, M. V. Berry, *J. Phys. A* **19**, 669 (1986).
- M. Kerker, *The Scattering of Light* (Academic Press, New York, 1969).
- I am grateful to L. Boussiakou, L. Davila-Romero, M. Dennis, M. Dunn, G. Gbur, C. Gibson, J. Henn, and A. Hindi for the discussions that led to this paper. My work has been supported by the Leverhulme Trust and the Engineering and Physical Sciences Research Council.

21 February 2006; accepted 26 April 2006

Published online 25 May 2006;

10.1126/science.1126493

Include this information when citing this paper.

Controlling Electromagnetic Fields

J. B. Pendry,^{1*} D. Schurig,² D. R. Smith²

Using the freedom of design that metamaterials provide, we show how electromagnetic fields can be redirected at will and propose a design strategy. The conserved fields—electric displacement field \mathbf{D} , magnetic induction field \mathbf{B} , and Poynting vector \mathbf{S} —are all displaced in a consistent manner. A simple illustration is given of the cloaking of a proscribed volume of space to exclude completely all electromagnetic fields. Our work has relevance to exotic lens design and to the cloaking of objects from electromagnetic fields.

To exploit electromagnetism, we use materials to control and direct the fields: a glass lens in a camera to produce an image, a metal cage to screen sensitive equipment, “blackbodies” of various forms to prevent unwanted reflections. With homogeneous materials, optical design is largely a matter of choosing the interface between two materials. For example, the lens of a camera is optimized by altering its shape so as to minimize geometrical aberrations. Electromagnetically inhomogeneous materials offer a different approach to control light; the introduction of specific gradients in the refractive index of a material can be used to form lenses and other optical elements, although the types and ranges of such gradients tend to be limited.

A new class of electromagnetic materials (1, 2) is currently under study: metamaterials, which owe their properties to subwavelength details of structure rather than to their chemical composition, can be designed to have properties difficult or impossible to find in nature. We show how the design flexibility of metamaterials can be used to achieve new electromagnetic devices and how metamaterials enable a new

paradigm for the design of electromagnetic structures at all frequencies from optical down to DC.

Progress in the design of metamaterials has been impressive. A negative index of refraction (3) is an example of a material property that does not exist in nature but has been enabled by using metamaterial concepts. As a result, negative refraction has been much studied in recent years (4), and realizations have been reported at both GHz and optical frequencies (5–8). Novel magnetic properties have also been reported over a wide spectrum of frequencies. Further information on the design and construction of metamaterials may be found in (9–13). In fact, it is now conceivable that a material can be constructed whose permittivity and permeability values may be designed to vary independently and arbitrarily throughout a material, taking positive or negative values as desired.

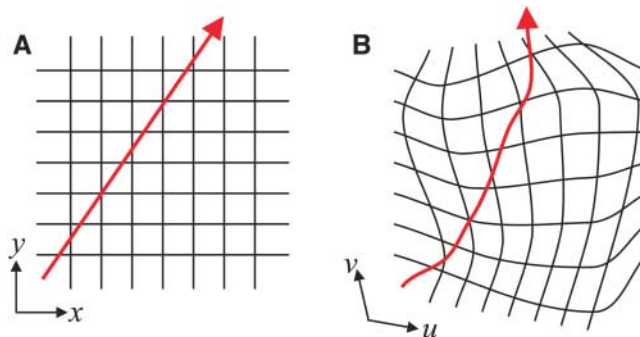


Fig. 1. (A) A field line in free space with the background Cartesian coordinate grid shown. (B) The distorted field line with the background coordinates distorted in the same fashion. The field in question may be the electric displacement fields \mathbf{D} or \mathbf{B} , or the Poynting vector \mathbf{S} , which is equivalent to a ray of light.

¹Department of Physics, Blackett Laboratory, Imperial College London, London SW7 2AZ, UK. ²Department of Electrical and Computer Engineering, Duke University, Box 90291, Durham, NC 27708, USA.

*To whom correspondence should be addressed. E-mail: j.pendry@imperial.ac.uk

If we take this unprecedented control over the material properties and form inhomogeneous composites, we enable a powerful form of electromagnetic design. As an example of this design methodology, we show how the conserved quantities of electromagnetism—the electric displacement field \mathbf{D} , the magnetic field intensity \mathbf{B} , and the Poynting vector \mathbf{S} —can all be directed at will, given access to the appropriate metamaterials. In particular, these fields can be focused as required or made to avoid objects and flow around them like a fluid, returning undisturbed to their original trajectories. These conclusions follow from exact manipulations of Maxwell’s equations and are not confined to a ray approximation. They encompass in principle all forms of electromagnetic phenomena on all length scales.

We start with an arbitrary configuration of sources embedded in an arbitrary dielectric and magnetic medium. This initial configuration would be chosen to have the same topology as the final result we seek. For example, we might start with a uniform electric field and require that the field lines be moved to avoid a given region. Next, imagine that the system is embedded in some elastic medium that can be pulled and stretched as we desire (Fig. 1). To keep track of distortions, we record the initial configuration of the fields on a Cartesian mesh, which is subsequently distorted by the same pulling and stretching process. The distortions can now be recorded as a coordinate transformation between the original Cartesian mesh and the distorted mesh

$$u(x, y, z), v(x, y, z), w(x, y, z) \quad (1)$$

where (u, v, w) is the location of the new point with respect to the $x, y,$ and z axes. What happens to Maxwell’s equations when we substitute the new coordinate system? The equations have exactly the same form in any coordinate system, but the refractive index—or more exactly the permittivity ϵ and permeability μ —are scaled by a common factor. In the new coordinate system,

we must use renormalized values of the permittivity and permeability:

$$\epsilon'_{uu} = \epsilon_u \frac{Q_u Q_v Q_w}{Q_u^2},$$

$$\mu'_{uu} = \mu_u \frac{Q_u Q_v Q_w}{Q_u^2}, \text{ etc.} \quad (2)$$

$$E'_{uu} = Q_u E_u, H'_{uu} = Q_u H_u, \text{ etc.} \quad (3)$$

where,

$$Q_u^2 = \left(\frac{\partial x}{\partial u}\right)^2 + \left(\frac{\partial y}{\partial u}\right)^2 + \left(\frac{\partial z}{\partial u}\right)^2$$

$$Q_v^2 = \left(\frac{\partial x}{\partial v}\right)^2 + \left(\frac{\partial y}{\partial v}\right)^2 + \left(\frac{\partial z}{\partial v}\right)^2$$

$$Q_w^2 = \left(\frac{\partial x}{\partial w}\right)^2 + \left(\frac{\partial y}{\partial w}\right)^2 + \left(\frac{\partial z}{\partial w}\right)^2 \quad (4)$$

As usual,

$$\mathbf{B}' = \mu_0 \mu' \mathbf{H}', \quad \mathbf{D}' = \epsilon_0 \epsilon' \mathbf{E}' \quad (5)$$

We have assumed orthogonal coordinate systems for which the formulae are particularly simple. The general case is given in (14) and in the accompanying online material (15). The equivalence of coordinate transformations and changes to ϵ and μ has also been referred to in (16).

Now let us put these transformations to use. Suppose we wish to conceal an arbitrary object contained in a given volume of space; furthermore, we require that external observers be unaware that something has been hidden from them. Our plan is to achieve concealment by cloaking the object with a metamaterial whose function is to deflect the rays that would have struck the object, guide them around the object, and return them to their original trajectory.

Our assumptions imply that no radiation can get into the concealed volume, nor can any radiation get out. Any radiation attempting to penetrate the secure volume is smoothly guided around by the cloak to emerge traveling in the

same direction as if it had passed through the empty volume of space. An observer concludes that the secure volume is empty, but we are free to hide an object in the secure space. An alternative scheme has been recently investigated for the concealment of objects (17), but it relies on a specific knowledge of the shape and the material properties of the object being hidden. The electromagnetic cloak and the object concealed thus form a composite whose scattering properties can be reduced in the lowest order approximation: If the object changes, the cloak must change, too. In the scheme described here, an arbitrary object may be hidden because it remains untouched by external radiation. The method leads, in principle, to a perfect electromagnetic shield, excluding both propagating waves and near-fields from the concealed region.

For simplicity, we choose the hidden object to be a sphere of radius R_1 and the cloaking region to be contained within the annulus $R_1 < r < R_2$. A simple transformation that achieves the desired result can be found by taking all fields in the region $r < R_2$ and compressing them into the region $R_1 < r < R_2$,

$$r' = R_1 + r(R_2 - R_1)/R_2,$$

$$\theta' = \theta,$$

$$\phi' = \phi \quad (6)$$

Applying the transformation rules (15) gives the following values: for $r < R_1$, ϵ' and μ' are free to take any value without restriction and do not contribute to electromagnetic scattering; for $R_1 < r < R_2$

$$\epsilon'_{r'} = \mu'_{r'} = \frac{R_2}{R_2 - R_1} \frac{(r' - R_1)^2}{r'},$$

$$\epsilon'_{\theta'} = \mu'_{\theta'} = \frac{R_2}{R_2 - R_1},$$

$$\epsilon'_{\phi'} = \mu'_{\phi'} = \frac{R_2}{R_2 - R_1} \quad (7)$$

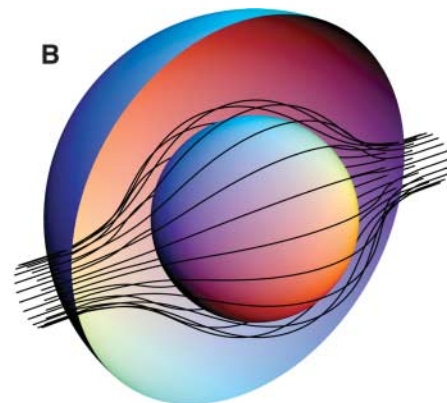
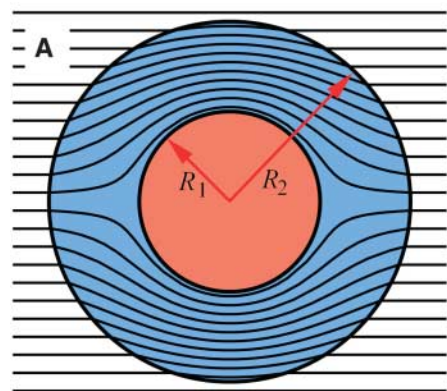


Fig. 2. A ray-tracing program has been used to calculate ray trajectories in the cloak, assuming that $R_2 \gg \lambda$. The rays essentially following the Poynting vector. (A) A two-dimensional (2D) cross section of rays striking our system, diverted within the annulus of cloaking material contained within $R_1 < r < R_2$ to emerge on the far side undeviated from their original course. (B) A 3D view of the same process.

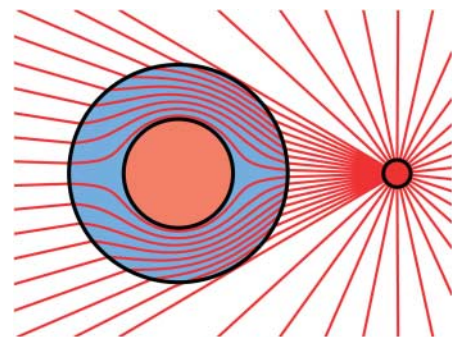


Fig. 3. A point charge located near the cloaked sphere. We assume that $R_2 \ll \lambda$, the near-field limit, and plot the electric displacement field. The field is excluded from the cloaked region, but emerges from the cloaking sphere undisturbed. We plot field lines closer together near the sphere to emphasize the screening effect.

for $r > R_2$

$$\epsilon'_{r'} = \mu'_{r'} = \epsilon'_{\theta'} = \mu'_{\theta'} = \epsilon'_{\phi'} = \mu'_{\phi'} = 1 \quad (8)$$

We stress that this prescription will exclude all fields from the central region. Conversely, no fields may escape from this region. At the outer surface of the cloak ($r = R_2$), we have $\epsilon'_{\theta'} = \epsilon'_{\phi'} = 1/\epsilon'_{r'}$ and $\mu'_{\theta'} = \mu'_{\phi'} = 1/\mu'_{r'}$, which are the conditions for a perfectly matched layer (PML). Thus we can make the connection between this cloak, which is reflectionless by construction, and a well-studied reflectionless interface (18).

For purposes of illustration, suppose that $R_2 \gg \lambda$, where λ is the wavelength, so that we can use the ray approximation to plot the Poynting vector. If our system is then exposed to a source of radiation at infinity, we can perform the ray-tracing exercise shown in Fig. 2. Rays in this figure result from numerical integration of a set of Hamilton's equations obtained by taking the geometric limit of Maxwell's equations with anisotropic, inhomogeneous media. This integration provides independent confirmation that the configuration specified by Eqs. 6 and 7 excludes rays from the interior region. Alternatively, if $R_2 \ll \lambda$ and we locate a point charge nearby, the electrostatic (or magnetostatic) approximation applies. A plot of the local electrostatic displacement field is shown in Fig. 3.

Next we discuss the characteristics of the cloaking material. There is an unavoidable singularity in the ray tracing, as can be seen by considering a ray headed directly toward the center of the sphere (Fig. 2). This ray does not know whether to be deviated up or down, left or right. Neighboring rays are bent around in tighter and tighter arcs the closer to the critical ray they are. This in turn implies very rapid changes in ϵ' and μ' , as sensed by the ray. These rapid changes are due (in a self-consistent way) to the tight turn of the ray and the anisotropy of ϵ' and μ' . Anisotropy of the medium is necessary because we have compressed space anisotropically.

Although anisotropy and even continuous variation of the parameters is not a problem for metamaterials (19–21), achieving very large or very small values of ϵ' and μ' can be. In practice, cloaking will be imperfect to the degree that we fail to satisfy Eq. 7. However, very considerable reductions in the cross section of the object can be achieved.

A further issue is whether the cloaking effect is broadband or specific to a single frequency. In the example we have given, the effect is only achieved at one frequency. This can easily be seen from the ray picture (Fig. 2). Each of the rays intersecting the large sphere is required to follow a curved, and therefore longer, trajectory than it would have done in free space, and yet we are requiring the ray to arrive on the far side of the sphere with the same phase. This implies a phase velocity greater than the velocity of light in vacuum which violates no physical law.

However, if we also require absence of dispersion, the group and phase velocities will be identical, and the group velocity can never exceed the velocity of light. Hence, in this instance the cloaking parameters must disperse with frequency and therefore can only be fully effective at a single frequency. We mention in passing that the group velocity may sometimes exceed the velocity of light (22) but only in the presence of strong dispersion. On the other hand, if the system is embedded in a medium having a large refractive index, dispersion may in principle be avoided and the cloaking operate over a broad bandwidth.

We have shown how electromagnetic fields can be dragged into almost any desired configuration. The distortion of the fields is represented as a coordinate transformation, which is then used to generate values of electrical permittivity and magnetic permeability ensuring that Maxwell's equations are still satisfied. The new concept of metamaterials is invoked, making realization of these designs a practical possibility.

References and Notes

1. J. B. Pendry, A. J. Holden, W. J. Stewart, I. Youngs, *Phys. Rev. Lett.* **76**, 4773 (1996).
2. J. B. Pendry, A. J. Holden, D. J. Robbins, W. J. Stewart, *IEEE Trans. Microw. Theory Techniques* **47**, 2075 (1999).
3. V. G. Veselago, *Soviet Physics USPEKI* **10**, 509 (1968).
4. D. R. Smith, W. J. Padilla, D. C. Vier, S. C. Nemat-Nasser, S. Schultz, *Phys. Rev. Lett.* **84**, 4184 (2000).
5. R. A. Shelby, D. R. Smith, S. Schultz, *Science* **292**, 77 (2001).
6. A. A. Houck, J. B. Brock, I. L. Chuang, *Phys. Rev. Lett.* **90**, 137401 (2003).
7. A. Grbic, G. V. Eleftheriades, *Phys. Rev. Lett.* **92**, 117403 (2004).

8. V. M. Shalaev *et al.*, *Opt. Lett.* **30**, 3356 (2005).
9. D. R. Smith, J. B. Pendry, M. C. K. Wiltshire, *Science* **305**, 788 (2004).
10. E. Cubukcu, K. Aydin, E. Ozbay, S. Foteinopoulou, C. M. Soukoulis, *Nature* **423**, 604 (2003).
11. E. Cubukcu, K. Aydin, E. Ozbay, S. Foteinopoulou, C. M. Soukoulis, *Phys. Rev. Lett.* **91**, 207401 (2003).
12. T. J. Yen *et al.*, *Science* **303**, 1494 (2004).
13. S. Linden *et al.*, *Science* **306**, 1351 (2004).
14. A. J. Ward, J. B. Pendry, *J. Mod. Opt.* **43**, 773 (1996).
15. Methods are available as supporting material on *Science Online*.
16. U. Leonhardt, *IEEE J. Selected Topics Quantum Electronics* **9**, 102 (2003).
17. A. Alu, N. Engheta, *Phys. Rev. E* **95**, 016623 (2005).
18. J.-P. Berenger, *J. Comput. Phys.* **114**, 185 (1994).
19. D. R. Smith, J. J. Mock, A. F. Starr, D. Schurig, *Phys. Rev. E* **71**, 036617 (2005).
20. T. Driscoll *et al.*, *Appl. Phys. Lett.* **88**, 081101 (2006).
21. R. B. Greegor *et al.*, *Appl. Phys. Lett.* **87**, 091114 (2005).
22. R. Y. Chiao, P. W. Milonni, *Optics and Photonics News*, June (2002).
23. J.B.P. thanks the Engineering and Physical Sciences Research Council (EPSRC) for a Senior Fellowship, the European Community (EC) under project FP6-NMP4-CT-2003-505699, Department of Defense Office of Naval Research (DOD/ONR) Multidisciplinary Research Program of the University Research Institute (MURI) grant N00014-01-1-0803, DOD/ONR grant N00014-05-1-0861, and the EC Information Societies Technology (IST) program Development and Analysis of Left-Handed Materials (DALHM), project number IST-2001-35511, for financial support. D. Schurig acknowledges support from the Intelligence Community (IC) Postdoctoral Fellowship Program.

Supporting Online Material

www.sciencemag.org/cgi/content/full/1125907/DC1
SOM Text
Figs. S1 to S3

7 February 2006; accepted 26 April 2006

Published online 25 May 2006;

10.1126/science.1125907

Include this information when citing this paper.

Nanoassembly of a Fractal Polymer: A Molecular "Sierpinski Hexagonal Gasket"

George R. Newkome,^{1,2*} Pingshan Wang,¹ Charles N. Moorefield,¹ Tae Joon Cho,¹ Prabhu P. Mohapatra,¹ Sinan Li,³ Seok-Ho Hwang,¹ Olena Lukoyanova,⁵ Luis Echegoyen,⁵ Judith A. Palagallo,⁴ Violeta Iancu,⁶ Saw-Wai Hla⁶

Mathematics and art converge in the fractal forms that also abound in nature. We used molecular self-assembly to create a synthetic, nanometer-scale, Sierpinski hexagonal gasket. This non-dendritic, perfectly self-similar fractal macromolecule is composed of *bis*-terpyridine building blocks that are bound together by coordination to 36 Ru and 6 Fe ions to form a nearly planar array of increasingly larger hexagons around a hollow center.

Fractal constructs are based on the incorporation of identical motifs that repeat on differing size scales (*l*). Examples of fractal shapes in nature include clouds, trees, waves on a lake, the human circulatory system, and mountains, to mention but a few. The study of fractals has moved from the field of pure mathematics to descriptions of nature that, in turn, have inspired artistic design. More recently, chemists have incorporated the fractal form in molecular synthesis. Since 1985, molecular trees, which generally

branch in a binary (2) or ternary (3) pattern, have been synthesized with increasing size and structural complexity. Beyond their aesthetics, these dendrimers and hyperbranched materials (4) are now under study for use in a wide range of practical applications. However, treelike patterns are but one type of fractal composed of repeating geometrical figures. A porphyrin-based dendrimer (5) that uses porphyrins as branching centers has been prepared that incorporates the snakelike "kolam" fractal pattern described by Ascher (6).

23. D. Mann, thesis, Stanford University (2006).
 24. W. J. Liang *et al.*, *Nature* **411**, 665 (2001).
 25. P. Jarillo-Herrero *et al.*, *Phys. Rev. Lett.* **94**, 156802 (2005).
 26. W. Chen, A. V. Andreev, A. M. Tselik, D. Orgad, *Phys. Rev. Lett.* **101**, 246802 (2008).
 27. S. R. White, I. Affleck, D. J. Scalapino, *Phys. Rev. B* **65**, 165122 (2002).
 28. Because of the sensitivity of the exponent on the model used and the general difficulty of accurately estimating it, the agreement to theory may be somewhat fortuitous. For example, a recent study gives an alternative scaling exponent of $a = 2$ for the gap (26). Nevertheless, our data are described both quantitatively and qualitatively by the theoretical calculations of (10), and the exponent of 1.3 is within the range $a = 1 - 2$ of theoretically predicted values for all the theoretical works cited that include long-ranged Coulomb interactions (10–12, 26).
 29. S. De Franceschi *et al.*, *Phys. Rev. Lett.* **86**, 878 (2001).
 30. L. S. Levitov, A. M. Tselik, *Phys. Rev. Lett.* **90**, 016401 (2003).
 31. M. Garst, D. S. Novikov, A. Stern, L. I. Glazman, *Phys. Rev. B* **77**, 035128 (2008).
 32. We acknowledge Micro Nano Laboratory at Caltech and Nanotech at the University of California, Santa Barbara where fabrication was performed. We thank A. Andreev,

D. Cobden, M. Garst, L. Glazman, S. Ilani, P. King, K. Le Hur, L. Levitov, G. Refael, and G. Steele for helpful discussions. M.B. and V.V.D. acknowledge the support of the Office of Naval Research, the Sloan Foundation, and the Ross Brown. D.N. was supported by NSF grants DMR-0749220 and DMR-0754613.

Supporting Online Material

www.sciencemag.org/cgi/content/full/323/5910/106/DC1
 Fig. S1

11 September 2008; accepted 20 November 2008
 10.1126/science.1165799

Broadband Invisibility by Non-Euclidean Cloaking

Ulf Leonhardt^{1,2*} and Tomáš Tyc^{2,3}

Invisibility and negative refraction are both applications of transformation optics where the material of a device performs a coordinate transformation for electromagnetic fields. The device creates the illusion that light propagates through empty flat space, whereas in physical space, light is bent around a hidden interior or seems to run backward in space or time. All of the previous proposals for invisibility require materials with extreme properties. Here we show that transformation optics of a curved, non-Euclidean space (such as the surface of a virtual sphere) relax these requirements and can lead to invisibility in a broad band of the spectrum.

Geometry has always played a distinguished role in optics (1), but direct optical applications of differential geometry are rather recent (2–4). Most notably, electromagnetic cloaking devices (5) are inspired by ideas of transformation optics (6–10), whereby transparent materials mimic coordinate transformations, forcing light to follow curved coordinates. The coordinates may enclose a hidden space, making the interior invisible and the act of cloaking undetectable. Another application of transformation optics (3, 4) is negative refraction (11, 12), where light follows coordinates that run backward in space (2) or time (13). One can also create optical analogs of the event horizon (2, 3, 14) and perhaps even electromagnetic wormholes (15). The key to engineering practical implementations of ideas that normally belong to general relativity (2–4) is the application of modern metamaterials (16–19). In metamaterials, man-made subwavelength structures generate unusual electromagnetic and optical properties. Metamaterials are potentially very versatile, but they are still subject to fundamental limits.

Take, for instance, the cloaking device (10) with the coordinate transformation illustrated in Fig. 1. The coordinates of physical space (Fig. 1B) are curved transformations of straight Car-

tesian coordinates in a virtual space that we call electromagnetic space (2) (Fig. 1A). This space is empty, so light follows straight lines that appear curved in physical space. If the coordinate transformation expands one point in electromagnetic space to an extended volume in physical space, anything in the “interior of the point” is invisible, as shown in Fig. 1B. However, Fig. 1 also reveals a fundamental problem of such cloaking devices. In electromagnetic space, light passes a point in infinitely short time, but in physical space the point has become an extended region. Thus, light

must propagate along the inner lining of the cloak at infinite speed (2). In materials, including metamaterials, the phase velocity (I) of light may approach infinity, but only at discrete frequencies that correspond to resonances of the material’s constituents. Light with different frequencies (different colors) would not be cloaked but instead be distorted. Furthermore, the group velocity (I) tends to be zero at resonances: Light pulses would become glued to the device instead of traveling around it (20). Therefore, turning invisibility from a tantalizing idea into a practical broadband device requires a different approach.

So far, transformation optics have mostly applied concepts of only Euclidean, flat space, the curved light rays being mere coordinate transformations of a space that is inherently flat. Here we explain how concepts of non-Euclidean geometry (i.e., of intrinsically curved space) could pave the way to broadband invisibility. In curved space, light may propagate along closed loops or may avoid some regions altogether. Most transparent materials act as if they would curve the geometry of light (3); light focused by a lens, refracted in a water droplet, or bent in a mirage perceives space as being curved, in general. Transformation media where the perceived space is inherently flat are the exceptions (3). However, to

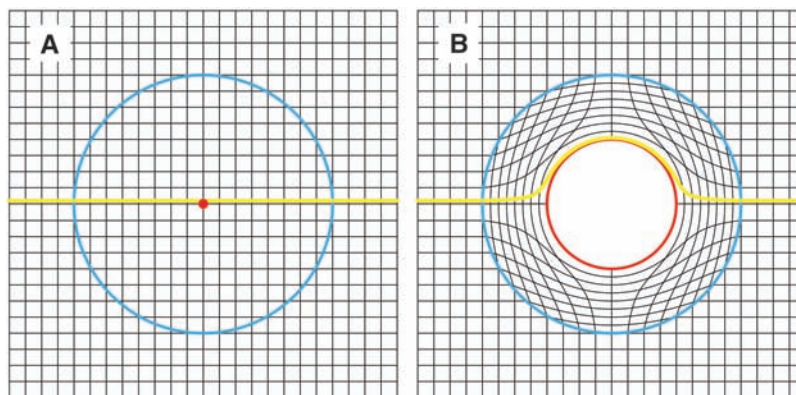


Fig. 1. Euclidean cloaking device (10). The device performs a coordinate transformation from the virtual space (A) to physical space (B). The virtual space is empty and flat (Euclidean). Because the curved coordinate lines of physical space are transformations of straight lines, physical space is Euclidean as well. The device creates the illusion that light propagates through flat space that is empty, apart from one point that, in physical space, has been expanded to finite size. The interior of the expanded point is hidden. Light, however, passes a point in infinitely short time. So, in physical space, the speed of light in the material of the device must approach infinity, which severely limits the use of Euclidean cloaking (10).

¹Physics Department, National University of Singapore, 2 Science Drive 3, Singapore 117542, Singapore. ²School of Physics and Astronomy, University of St. Andrews, North Haugh, St. Andrews, KY16 9SS, UK. ³Institute of Theoretical Physics and Astrophysics, Masaryk University, Kotlarska 2, 61137 Brno, Czech Republic.

*To whom correspondence should be addressed. E-mail: ulf@st-andrews.ac.uk

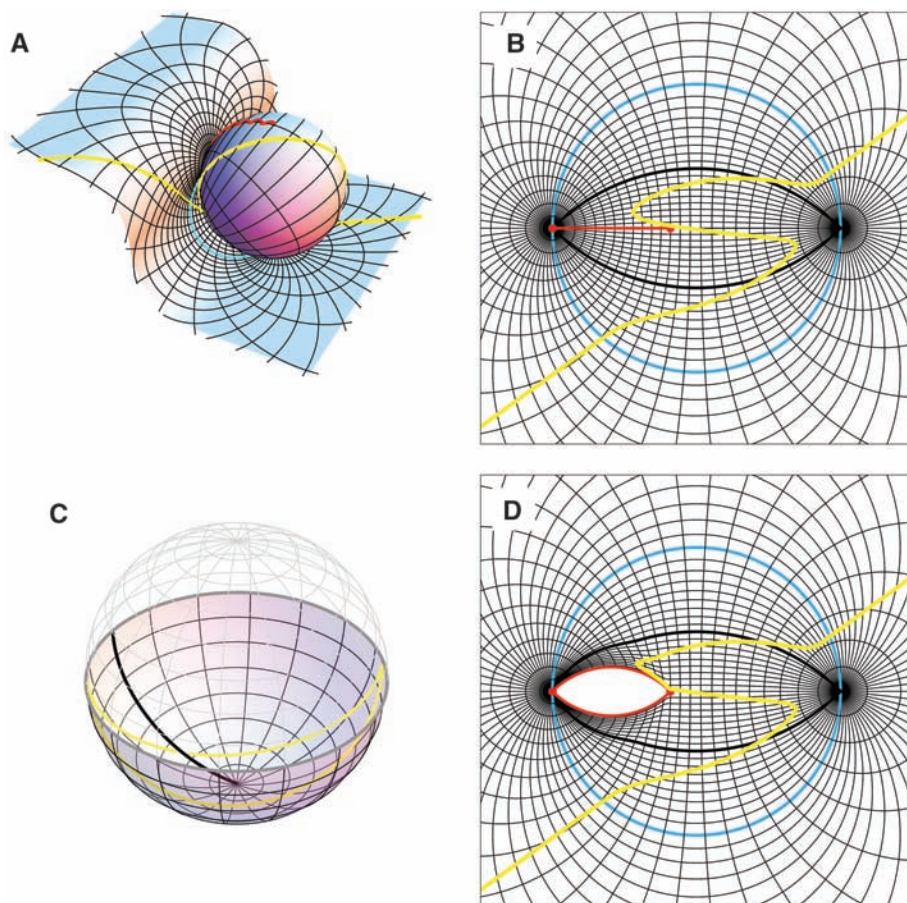


Fig. 2. Non-Euclidean cloaking device in two dimensions. The device creates the illusion shown in (A): Light propagates through a virtual space that consists of a plane and the surface of a sphere, a curved space, which touch along a line. Some incident light rays venture from the plane to the sphere; they return after one loop around the equator of the globe (Fig. 2C), light is reflected twice, creating the illusion of following a great circle, yet never reaching the northern hemisphere. Anything placed inside the corresponding area in physical space is invisible. A more elegant option instead of hiding behind a mirror is the creation of an invisible space that light naturally avoids (22). For example, the light circles on the sphere never cross the red zigzag shown in Fig. 2A. Imagine we open the zigzag like a zip in physical space (Fig. 2D). Anything inside this region is hidden, and the act of hiding is not detectable on the light rays: We have a cloaking device. On the other hand, light performs loops on the sphere, which takes time. Measuring time delays or examining the phase fronts of light rays could reveal the presence of the cloaking device. This imperfection (9, 22) is the price to pay for practical invisibility, whereas perfect invisibility (10) is not practical.

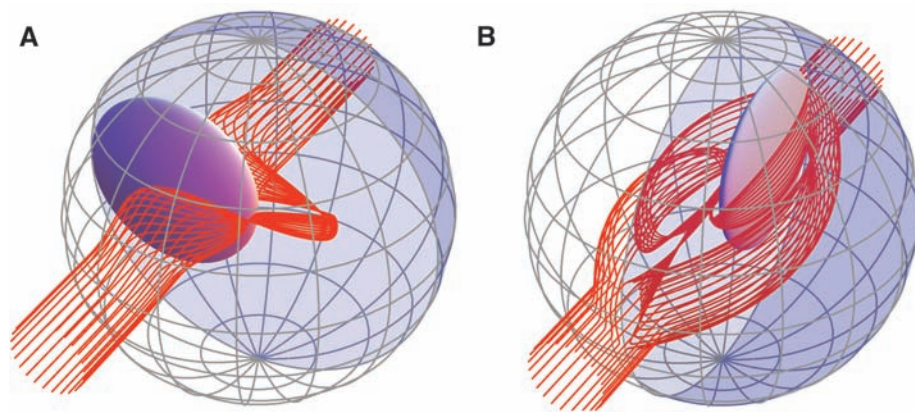


Fig. 3. 3D cloaking. One can extrapolate the ideas illustrated in Fig. 2 to 3D space, replacing the plane by flat space and the sphere by a hypersphere. The lentil-shaped object indicates the hidden interior of the device, and the partly shaded grid denotes the boundary of the invisibility device. For better contrast, light rays are shown in red. (A) Rays are bent around the invisible region. (B) In three dimensions, some rays turn out to perform two loops in hyperspace that appear in physical space as light wrapped around the invisible interior.

achieve invisibility, it is necessary to curve the geometry in specific ways.

We explain our ideas with pictures, the complete calculations behind the pictures being described in the supporting online material (21). As three-dimensional (3D) curved space is difficult to visualize, we first explain our concept on a 2D example and then extend this case to three dimensions. Figure 2A shows the archetype of a non-Euclidean space (the surface of a sphere) combined with a Euclidean space (the plane) that touches the sphere like a piece of paper partially wrapped around a globe. Both the plane and the sphere carry a coordinate grid that we map onto physical space (the plane shown in Fig. 2B). The entrance to the sphere (i.e., the line where the globe touches the plane) has been opened like an eye in the physical plane to make space for the grid of the sphere. In mathematical terminology, electromagnetic space consists of two branches, plane and sphere, that are connected at a branch cut. Although the globe has been flattened in physical space, the exterior curvature of the sphere is maintained as intrinsic curvature.

As there is a one-to-one correspondence between light propagation in the physical plane (Fig. 2B) and in electromagnetic space (Fig. 2A), we discuss the optics in electromagnetic space. Light rays follow geodesics (3), lines of shortest or longest path (1, 3). The geodesics on the sphere are the great circles. Light entering the sphere through the branch cut performs a loop and leaves in the same direction as before; the sphere is invisible but it does not make anything else invisible yet. However, if we place a mirror around the equator of the virtual sphere (C), making the northern hemisphere invisible and creating the same illusion as shown in (A). (D) Alternatively, one could expand the red line that light never crosses to create a hidden space.

The implementation of our idea does not demand extreme optical properties such as infinities or zeros of the speed of light, for the following reason: In electromagnetic space, light propagates at the speed of light in vacuum. Physical space represents a deformed image of electromagnetic space; the speed of light follows this deformation. Expressed in quantitative terms, if an infinitesimal line element in electromagnetic space is n times longer than its image in physical

space, then the refractive index in the corresponding direction in physical space is n . Figure 2 as well as calculations (21) show that the ratio of the line elements is neither infinite nor zero. Even at a branch point the spatial deformation in any direction is finite, because here the coordinate grid is only compressed in angular direction by a finite factor, in contrast to optical conformal mapping (9). Furthermore, the spatial deformations are gradual, for avoiding reflections at boundaries (23).

Figure 3 illustrates the extension of our idea to three dimensions. Instead of the 2D surface of the globe of Fig. 2A, we use the 3D surface of a 4D sphere (a hypersphere). Such a geometry is realized (24, 25) in Maxwell's fish eye (1, 26). Inside the cloaking device, we inflate a 2D surface, the branch cut in 3D, like a balloon to make space for the 3D surface of the hypersphere. Again, at this point the cloak is invisible but does not hide anything yet. Then we open another spatial branch on the "zip" of the hypersphere to create a hidden interior. The branch cuts are curved surfaces in electromagnetic space, which is the only important difference when compared with the 2D case. Some light rays may pierce the entrance to the hypersphere twice; they perform two loops in the non-Euclidean branch. In physical space, light is wrapped around the invisible interior in such cases (Fig. 3B). We calculated

the required electromagnetic properties (21) and found that the electric permittivity ranges from 0.28 to 31.2 for our specific example. One could give the cloaking device any desired shape by further coordinate transformations, which would change the requirements on the optical properties of the material. As a rule, the larger the cloaked fraction of the total volume of the device, the stronger the optics of the material must be, but the required speed of light will always remain finite.

References and Notes

- M. Born, E. Wolf, *Principles of Optics* (Cambridge Univ. Press, Cambridge, 1999).
- U. Leonhardt, T. G. Philbin, *New J. Phys.* **8**, 247 (2006).
- U. Leonhardt, T. G. Philbin, in press; preprint available at <http://arxiv.org/abs/0805.4778> (2008).
- V. M. Shalaev, *Science* **322**, 384 (2008).
- D. Schurig *et al.*, *Science* **314**, 977 (2006), published online 18 October 2006; 10.1126/science.1133628.
- An early precursor of transformation optics is (7).
- L. S. Dolin, *Izvestiya Vusov* **4**, 964 (1961).
- A. Greenleaf, M. Lassas, G. Uhlmann, *Math. Res. Lett.* **10**, 1 (2003).
- U. Leonhardt, *Science* **312**, 1777 (2006), published online 24 May 2006; 10.1126/science.1126493.
- J. B. Pendry, D. Schurig, D. R. Smith, *Science* **312**, 1780 (2006), published online 24 May 2006; 10.1126/science.1125907.
- J. Yao *et al.*, *Science* **321**, 930 (2008).
- J. Valentine *et al.*, *Nature* **455**, 376 (2008).
- J. B. Pendry, *Science* **322**, 71 (2008), published online 28 August 2008; 10.1126/science.1162087.

- T. G. Philbin *et al.*, *Science* **319**, 1367 (2008).
- A. Greenleaf, Y. Kurylev, M. Lassas, G. Uhlmann, *Phys. Rev. Lett.* **99**, 183901 (2007).
- G. W. Milton, *The Theory of Composites* (Cambridge Univ. Press, Cambridge, 2002).
- D. R. Smith, J. B. Pendry, M. C. K. Wiltshire, *Science* **305**, 788 (2004).
- C. M. Soukoulis, S. Linden, M. Wegener, *Science* **315**, 47 (2007).
- A. K. Sarychev, V. M. Shalaev, *Electrodynamics of Metamaterials* (World Scientific, Singapore, 2007).
- H. Chen, C. T. Chan, *J. Appl. Phys.* **104**, 033113 (2008).
- See the supporting material on *Science* Online.
- U. Leonhardt, *New J. Phys.* **8**, 118 (2006).
- W. S. Cai, U. K. Chettiar, A. V. Kildishev, V. M. Shalaev, G. W. Milton, *Appl. Phys. Lett.* **91**, 111105 (2007).
- R. K. Luneburg, *Mathematical Theory of Optics* (Univ. of California Press, Berkeley, CA, 1964).
- H. A. Buchdahl, *Am. J. Phys.* **46**, 840 (1978).
- J. C. Maxwell, *Cambridge Dublin Math. J.* **8**, 188 (1854).
- We thank N. V. Korolkova for her generous support of this work. We are grateful for funding from European Union Contract Computing with Mesoscopic Photonic and Atomic States, the grants MSM0021622409 and MSM0021622419, and a Royal Society Wolfson Research Merit Award.

Supporting Online Material

www.sciencemag.org/cgi/content/full/1166332/DC1
SOM Text

Figs. S1 to S15

References

23 September 2008; accepted 5 November 2008

Published online 20 November 2008;

10.1126/science.1166332

Include this information when citing this paper.

Control of Self-Assembly of DNA Tubules Through Integration of Gold Nanoparticles

Jaswinder Sharma,^{1,2*} Rahul Chhabra,^{1,2*} Anchi Cheng,³ Jonathan Brownell,³ Yan Liu,^{1,2†} Hao Yan^{1,2†}

The assembly of nanoparticles into three-dimensional (3D) architectures could allow for greater control of the interactions between these particles or with molecules. DNA tubes are known to form through either self-association of multi-helix DNA bundle structures or closing up of 2D DNA tile lattices. By the attachment of single-stranded DNA to gold nanoparticles, nanotubes of various 3D architectures can form, ranging in shape from stacked rings to single spirals, double spirals, and nested spirals. The nanoparticles are active elements that control the preference for specific tube conformations through size-dependent steric repulsion effects. For example, we can control the tube assembly to favor stacked-ring structures using 10-nanometer gold nanoparticles. Electron tomography revealed a left-handed chirality in the spiral tubes, double-wall tube features, and conformational transitions between tubes.

Nanoparticles can exhibit distinctive electronic, magnetic, and photonic properties (1), and their assembly into well-defined

one-dimensional (1D), 2D, and 3D architectures with geometric controls could add to their functionality. DNA-mediated assembly of nanoparticles is an attractive way to organize both metallic and semiconducting nanoparticles into periodic or discrete 1D and 2D structures (1–14) through the programmable base-pairing interactions and the ability to construct branched DNA nanostructures of various geometries. Recent success in using DNA as a molecular glue to direct gold nanoparticles (AuNPs) into periodic 3D crystalline lattices further demonstrates the

power of DNA as building blocks for 3D nano-engineering (15, 16).

Here, we report a group of complex 3D geometric architectures of AuNPs created using DNA tile-mediated self-assembly. These are tubular nanostructures with various conformations and chiralities resembling those of carbon nanotubes. The nanoparticle tube assembly can be engineered both by the underlying DNA tile scaffolds and the nanoparticles themselves. Previous work in structural DNA nanotechnology has shown that DNA tubes can form through either the self-association of multi-helix DNA bundle structures or the closing up of 2D DNA tile lattices (17–26). The forces that drive tube formation have been attributed to the intrinsic curvature of the tile-array (21) and the thermodynamic requirement to lower the free energy of the system by minimizing the number of unpaired sticky ends (22). The intrinsic dimensional anisotropy of the DNA tiles also plays an important role in the kinetic control of the tube growth (26).

In all of the above studies, the true 3D conformations of DNA tubes have never been revealed in detail because of limitations in microscopic imaging techniques; deposition of the samples on a surface for atomic force microscope (AFM) or transmission electron microscope (TEM) imaging usually causes flattening and sometimes opening of the tubes. This limitation has prevented a comprehensive understanding of the structural features of DNA nanotubes. For example, the handedness of the chiral tubes can be better revealed with 3D structural characteriza-

¹Center for Single Molecule Biophysics, The Biodesign Institute, Arizona State University, Tempe, AZ 85287, USA.

²Department of Chemistry and Biochemistry, Arizona State University, Tempe, AZ 85287, USA. ³National Resource for Automated Molecular Microscopy, The Scripps Research Institute, La Jolla, CA 92037, USA.

*These authors contributed equally to this work.

†To whom correspondence should be addressed. E-mail: hao.yan@asu.edu (H.Y.); yan_liu@asu.edu (Y.L.)

Magnifying Superlens in the Visible Frequency Range

Igor I. Smolyaninov,* Yu-Ju Hung, Christopher C. Davis

We demonstrate a magnifying superlens that can be integrated into a conventional far-field optical microscope. Our design is based on a multilayer photonic metamaterial consisting of alternating layers of positive and negative refractive index, as originally proposed by Narimanov and Engheta. We achieved a resolution on the order of 70 nanometers. The use of such a magnifying superlens should find numerous applications in imaging.

Optical microscopy is an invaluable tool for studies of materials and biological entities. Imaging tools with ever-increasing spatial resolution are required if the current rate of progress in nanotechnology and microbiology is to continue. However, the spatial resolution of conventional microscopy is limited by the diffraction of light waves to a value on the order of 200 nm. Thus, viruses, proteins, DNA molecules, and many other samples are impossible to visualize with a regular microscope. One suggested way to overcome this limitation is based on the concept of a superlens (1), which relies on the use of materials or metamaterials that have negative refractive index in the visible frequency range. Near-field superlens imaging was recently demonstrated (2, 3), but the technique is limited by the fact that the magnification of the planar superlens is equal to 1. Thus, a thin planar superlens cannot be integrated into a conventional optical microscope to image objects smaller than the diffraction limit.

We describe the realization of a magnifying superlens (Fig. 1A) and demonstrate its integration into a regular far-field optical microscope. Our design is based on the theo-

retical proposals of an “optical hyperlens” (4) and “metamaterial crystal lens” (5) and on the recently developed plasmon-assisted microscopy technique (6), and in particular on the unusual optics of surface plasmon polaritons (SPPs). The properties of these two-dimensional optical modes and convenient ways to excite them are described in detail in (7). The wave vector of the SPPs is defined by the expression

$$k_p = \frac{\omega}{c} \left(\frac{\epsilon_d \epsilon_m}{\epsilon_d + \epsilon_m} \right)^{1/2} \quad (1)$$

where $\epsilon_m(\omega)$ and $\epsilon_d(\omega)$ are the frequency-dependent dielectric constants of the metal and the dielectric, respectively, and c is the speed of light. Above the resonant frequency ω described by the condition

$$\epsilon_m(\omega) \approx -\epsilon_d(\omega) \quad (2)$$

the SPP group and phase velocities may have opposite signs (Fig. 1B). The internal structure of the magnifying superlens (Fig. 2A) consists of concentric rings of poly(methyl methacrylate) (PMMA) deposited on a gold film surface. For the SPP dispersion law for the gold-vacuum and gold-PMMA interfaces (Fig. 1B) in the frequency range marked by the box, PMMA has negative refractive index $n_2 < 0$ as perceived by plasmons (the group velocity is opposite to the

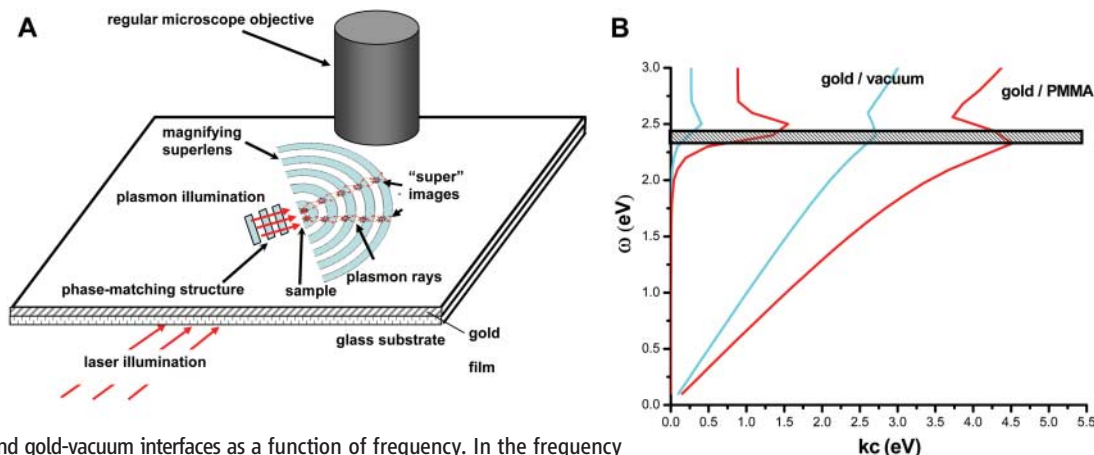
phase velocity). The width of the PMMA rings d_2 is chosen so that $n_1 d_1 = -n_2 d_2$, where d_1 is the width of the gold-vacuum portions of the interface. Although the imaging action of our lens is based on the original planar superlens idea, its magnification depends on the fact that all the rays in the superlens tend to propagate in the radial direction when $n_1 d_1 = -n_2 d_2$ (Fig. 1A). This behavior was observed in the experiment upon illumination of the lens with $\lambda = 495$ nm laser light (bottom portion of Fig. 2B) for which $n_1 d_1 = -n_2 d_2$. The narrow beam visible in the image is produced by repeating self-imaging of the focal point by the alternating layers of materials with positive and negative refractive index. On the other hand, if 515-nm light is used, the lens becomes uncompensated and the optical field distribution inside the lens reproduces the field distribution in the normal “plasmonic lens” as described in (8) (top portion of Fig. 2B). However, in the complete theoretical description of the magnifying superlens, the ray optics picture presented in Fig. 1A may need to be supplemented by the anisotropic effective medium theory presented in (4, 5).

The magnifying action of the superlens is demonstrated in Figs. 3 and 4. Rows of two or three PMMA dots were produced near the inner ring of the superlens (Fig. 3, B and C). These rows of PMMA dots had 0.5- μ m periodicity in the radial direction, so that phase matching between the incident laser light and surface plasmons could be achieved (Fig. 1A). Upon illumination with an external laser, the three rows of PMMA dots in Fig. 3B gave rise to three radial divergent plasmon “rays,” which are clearly visible in the plasmon image in Fig. 3D obtained with a conventional optical microscope. The cross-sectional analysis of this image across the plasmon “rays” (Fig. 3F) indicates resolution of at least 70 nm, or $\sim \lambda/7$. The lateral separation between these rays increased by a factor of 10 as the rays reached the outer rim of the superlens. This increase allowed visualization of the triplet by conventional microscopy. In

Department of Electrical and Computer Engineering, University of Maryland, College Park, MD 20742, USA.

*To whom correspondence should be addressed. E-mail: smoly@eng.umd.edu

Fig. 1. (A) Schematic of the magnifying superlens integrated into a conventional microscope. The plasmons generated by the phase-matching structure illuminate the sample positioned near the center of the superlens. The lateral distance between the images produced by the alternating layers of materials with positive and negative refractive index grows with distance along the radius. The magnified images are viewed by a regular microscope. (B) Real and imaginary parts of the surface plasmon wave vector k at the gold-PMMA and gold-vacuum interfaces as a function of frequency. In the frequency range marked by the box, PMMA has negative refractive index as perceived by plasmons, whereas the gold-vacuum interface looks like a medium with positive refractive index.



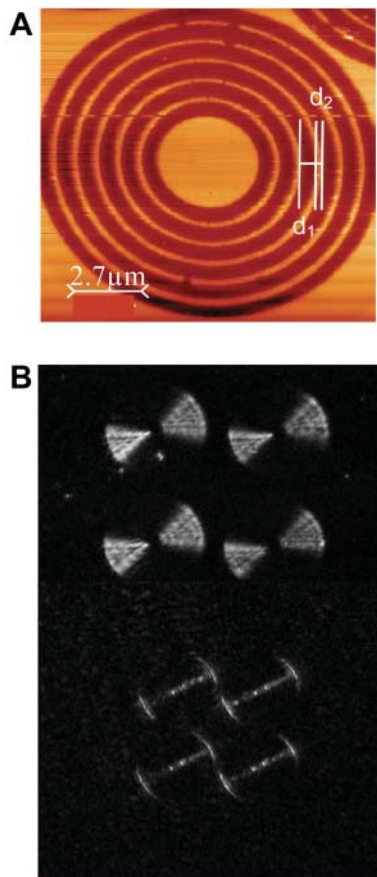


Fig. 2. (A) AFM image of the magnifying superlens made of PMMA rings on the gold film surface. (B) Optical field distribution in the magnifying superlens illuminated by external laser in the frequency ranges where $n_1 d_1 \neq -n_2 d_2$ (top) and $n_1 d_1 = -n_2 d_2$ (bottom).

a similar fashion, the two radial rows of PMMA dots shown in Fig. 3C gave rise to two plasmon rays, which are visualized in Fig. 3E.

The composite image in Fig. 4 is a superposition of the atomic force microscopy (AFM) image from Fig. 3A and the corresponding optical image obtained by conventional optical microscopy. It illustrates the imaging mechanism of the magnifying superlens: The passage of plasmon rays through the concentric alternating layers of materials with positive and negative refractive index increases the lateral separation of the three rays (marked by arrows at lower right). Near the edge of the superlens, the separation is large enough to be resolved with a conventional optical microscope, thus demonstrating a magnifying superlens in the visible frequency range.

The theoretical resolution of such a microscope may reach the nanometer scale (1, 4). It thus has the potential to become an invaluable tool in medical and biological imaging, where far-field optical imaging of individual viruses and DNA molecules may become a reality. It allows very simple, fast, robust, and straightforward image acquisition.

Fig. 3. AFM images (A to C) and conventional optical microscopy images (D and E) of the resolution test samples composed of three (A and B) and two (C) radial rows of PMMA dots (marked by arrows) positioned near the center of the magnifying superlens. The conventional microscopy images presented in (D) and (E) correspond to the samples shown in (B) and (C), respectively. The rows of PMMA dots give rise to either three or two divergent plasmon "rays" (marked by arrows) which are visible in the conventional optical microscopy images. (F) The cross section of the optical image along the line shown in (D) indicates resolution of at least 70 nm or $\sim \lambda/7$. Z, optical signal; X, distance.

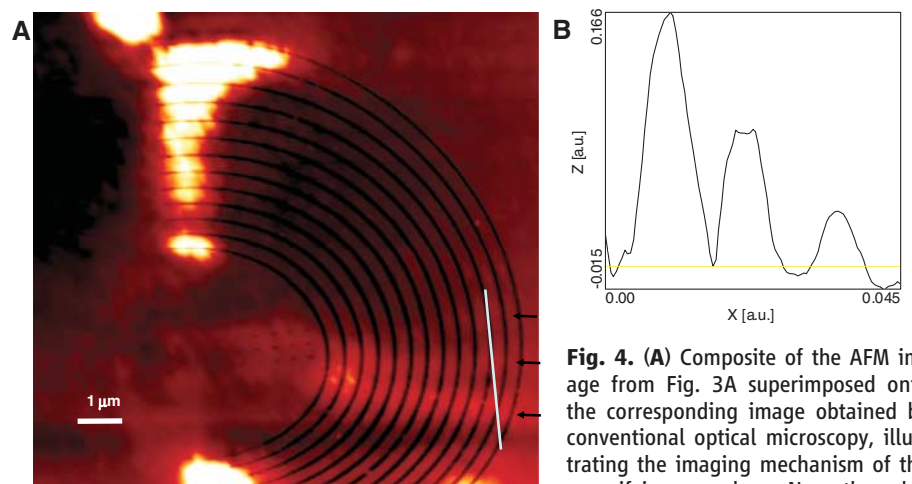
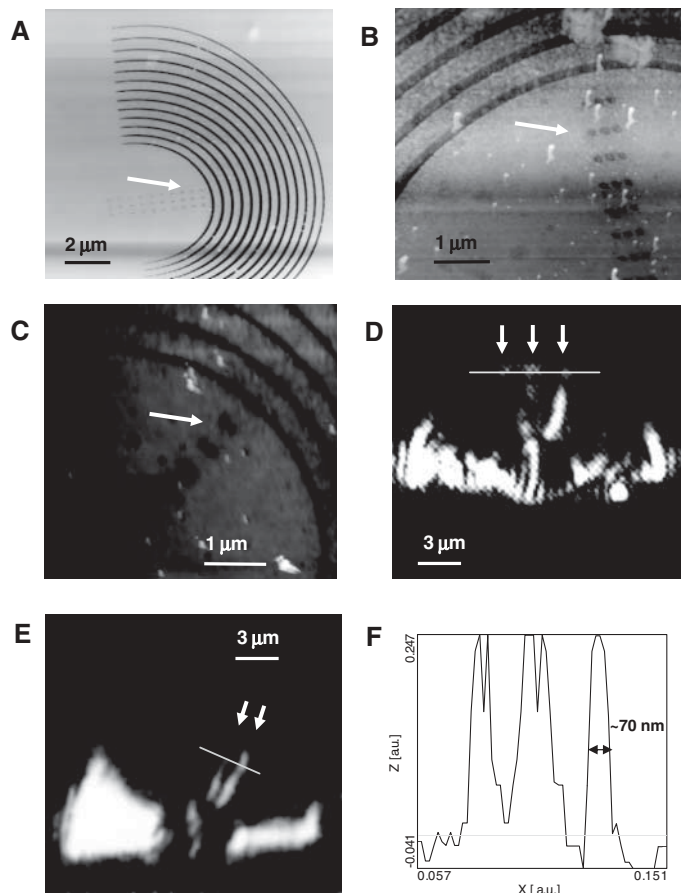


Fig. 4. (A) Composite of the AFM image from Fig. 3A superimposed onto the corresponding image obtained by conventional optical microscopy, illustrating the imaging mechanism of the magnifying superlens. Near the edge of the superlens, the separation of three rays (marked by arrows) is large enough to be resolved using a conventional optical microscope. (B) The cross section of the optical image along the line shown in (A) indicates the three rays.

We expect that unusual optical metamaterials may be designed and implemented using the principle of our magnifying superlens. Because $(d_1 + d_2)$ and the d_1/d_2 ratio (Fig. 2A) are easy to vary locally, the effective anisotropic refractive index of the multilayer material may be varied continuously from large negative to large positive values. Thus, unusual nanophotonic devices may be created in the visible

frequency range, such as the recently suggested (9, 10) and demonstrated (11) "invisibility cloak."

References and Notes

1. J. B. Pendry, *Phys. Rev. Lett.* **85**, 3966 (2000).
2. N. Fang, H. Lee, C. Sun, X. Zhang, *Science* **308**, 534 (2005).
3. D. O. S. Melville, R. J. Blaikie, *Opt. Express* **13**, 2127 (2005).

4. Z. Jacob, L. V. Alekseyev, E. Narimanov, *Opt. Express* **14**, 8247 (2006).
5. A. Salandrino, N. Engheta, *Phys. Rev. B* **74**, 075103 (2006).
6. I. I. Smolyaninov, C. C. Davis, J. Elliott, A. V. Zayats, *Phys. Rev. Lett.* **94**, 057401 (2005).
7. A. V. Zayats, I. I. Smolyaninov, A. A. Maradudin, *Phys. Rep.* **408**, 131 (2005).
8. Z. Liu, J. M. Steele, H. Lee, X. Zhang, *Appl. Phys. Lett.* **88**, 171108 (2006).
9. J. B. Pendry, D. Schurig, D. R. Smith, *Science* **312**, 1780 (2006); published online 24 May 2006 (10.1126/science.1125907).
10. U. Leonhardt, *Science* **312**, 1777 (2006); published online 24 May 2006 (10.1126/science.1126493).
11. D. Schurig *et al.*, *Science* **314**, 977 (2006); published online 18 October 2006 (10.1126/science.1133628).
12. Supported by NSF grants ECS-0304046 and CCF-0508213.

12 December 2006; accepted 8 February 2007
10.1126/science.1138746

Coupled Thermal and Hydrological Evolution of Tropical Africa over the Last Deglaciation

Johan W. H. Weijers,^{1*} Enno Schefuß,^{2†} Stefan Schouten,¹ Jaap S. Sinninghe Damsté¹

We analyzed the distribution of branched tetraether membrane lipids derived from soil bacteria in a marine sediment record that was recovered close to the Congo River outflow, and the results enabled us to reconstruct large-scale continental temperature changes in tropical Africa that span the past 25,000 years. Tropical African temperatures gradually increased from ~21° to 25°C over the last deglaciation, which is a larger warming than estimated for the tropical Atlantic Ocean. A direct comparison with sea-surface temperature estimates from the same core revealed that the land-sea temperature difference was, through the thermal pressure gradient, an important control on central African precipitation patterns.

Continental climate change during the last deglaciation, especially in the tropics, is not as well understood as it is for the oceans (1–3). For Africa, a consensus is emerging on past changes in humidity and their causes based on lake level and pollen studies as well as the deuterium content of plant waxes (4–6), but temperature records for such tropical continental areas remain scarce and incomplete. In contrast to the marine environment, few quantitative temperature proxies exist for the terrestrial environment, and continuous long-term climate archives on land are limited. For instance, pollen-based vegetation studies, a widely used method for environmental reconstructions on land (5), are complicated in the tropics because the effects of changes in temperature are difficult to distinguish from those of changes in precipitation. Temperature estimates based on another method, stable oxygen isotope contents of carbonates and silicates, are widely applied in lacustrine sediments and speleothems. However, although these estimates are appropriate for high-resolution qualitative paleoclimate reconstructions (7, 8), quantification of climate change in terms of paleotemperatures requires tenuous assumptions about the past changes in

parameters that have influenced the source-water composition. The scant paleotemperature data available for the African continent imply a temperature difference of ~3.5° to 6°C between the Last Glacial Maximum (LGM) and the present day (2, 5, 9, 10), but these data often represent a relatively local signal or are incomplete records. Thus, knowledge on African tropical temperature change over the last deglaciation is rather limited, especially for the vast tropical rainforest area of the Congo Basin. Continuous, high resolution, long-term records of continental-scale temperature change are much needed to improve this knowledge and enable proper comparison with records of marine temperature changes.

To gain better insight into the central African temperature development over the last deglaciation, its relation to global climatic changes, and its effect on the continental hydrological cycle, we used the Methylation index of Branched Tetraethers (MBT) and Cyclization ratio of Branched Tetraethers (CBT) based on branched glycerol dialkyl glycerol tetraethers (GDGTs) (11) present in a marine core recovered close to the Congo River outflow (GeoB 6518-1, 05°35.3'S, 11°13.3'E, water depth of 962 m, Fig. 1). Using the MBT and the CBT, we reconstructed the annual mean air temperature (MAT) of the Congo River basin (12) which could be compared with the sea surface temperature (SST) record obtained from the same core (Fig. 2). Branched GDGTs (fig. S1) are abundant core membrane lipids derived from bacteria that thrive in soils (11, 13, 14). As the soil erodes, the GDGTs are fluviually transported to the ocean. Indeed, they have been shown to be an excellent tracer of the fate of soil organic matter in the Congo deep-sea fan (13) and the Bay of Biscay (15) (fig. S2). The large catchment area of the Congo River (3.7 × 10⁶ km²) extends from about 6°N to 13°S and from about 13° to 33°E in central Africa (Fig. 1A), with elevations between 300 and 1200 m except for one small part, located at its eastern boundary, that rises above 2000 m (16). The temperature estimates obtained from our marine core, therefore, represent a catchment-integrated terrestrial temperature signal derived from land of low to intermediate elevation. Analysis of the

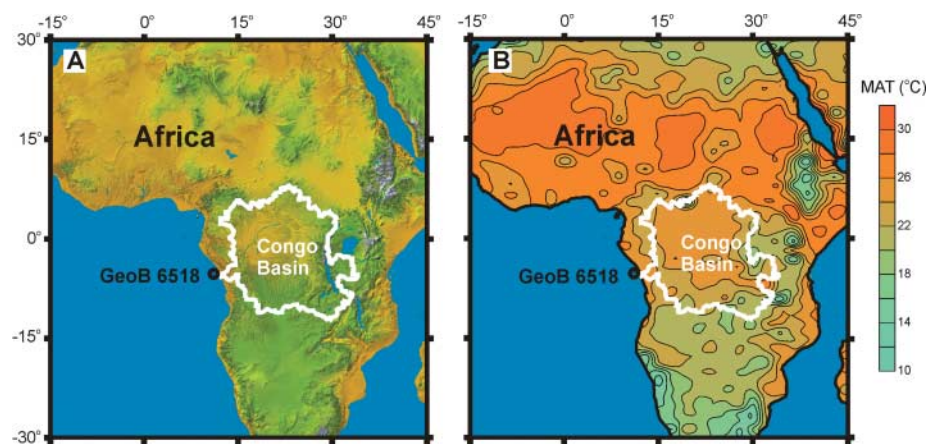


Fig. 1. Overview maps of Africa. The position of core GeoB 6518, recovered close to the Congo River outflow from a water depth of 962 m, and the extent of the Congo River drainage basin (white outline) are plotted (A) on a digital elevation map of Africa [picture from NASA Jet Propulsion Laboratory, California Institute of Technology] and (B) on a map showing the annual MAT distribution in Africa [available in the database in (30)].

¹Royal Netherlands Institute for Sea Research, Department of Marine Biogeochemistry and Toxicology, Post Office Box 59, 1790 AB Den Burg–Texel, Netherlands. ²Deutsche Forschungsgemeinschaft (DFG)–Research Center Ocean Margins, University of Bremen, Leobener Strasse, 28359 Bremen, Germany.

*To whom correspondence should be addressed. E-mail: jweijers@nioz.nl

†Present address: Institute for Geosciences, Christian-Albrechts-University Kiel, Ludewig-Meyn-Strasse 10, 28114 Kiel, Germany.

Acoustic cloaking theory

BY ANDREW N. NORRIS*

*Mechanical and Aerospace Engineering, Rutgers University,
Piscataway, NJ 08854-8058, USA*

An acoustic cloak is a compact region enclosing an object, such that sound incident from all directions passes through and around the cloak as though the object was not present. A theory of acoustic cloaking is developed using the transformation or change-of-variables method for mapping the cloaked region to a point with vanishing scattering strength. We show that the acoustical parameters in the cloak must be anisotropic: either the mass density or the mechanical stiffness or both. If the stiffness is isotropic, corresponding to a fluid with a single bulk modulus, then the inertial density must be infinite at the inner surface of the cloak. This requires an infinitely massive cloak. We show that perfect cloaking can be achieved with finite mass through the use of anisotropic stiffness. The generic class of anisotropic material required is known as a pentamode material (PM). If the transformation deformation gradient is symmetric then the PM parameters are explicit, otherwise its properties depend on a stress-like tensor that satisfies a static equilibrium equation. For a given transformation mapping, the material composition of the cloak is not uniquely defined, but the phase speed and wave velocity of the pseudo-acoustic waves in the cloak are unique. Examples are given from two and three dimensions.

Keywords: cloaking; pentamode; anisotropy

1. Introduction

The observation that the electromagnetic equations remain invariant under spatial transformations is not new. Ward & Pendry (1996) used it for numerical purposes, but the result was known to Post (1962) who discussed it in his book, and it was probably known far earlier. The recent interest in passive cloaking and invisibility is due to the fundamental result of Greenleaf *et al.* (2003*a,b*) that singular transformations could lead to cloaking for conductivity. Not long after this important discovery Leonhardt (2006) and Pendry *et al.* (2006) made the key observation that singular transformations could be used to achieve cloaking of electromagnetic waves. These results and others have generated significant interest in the possibility of passive acoustic cloaking.

Acoustic cloaking is considered here in the context of the so-called transformation or change-of-variables method. The transformation deforms a region in such a way that the mapping is one-to-one everywhere except at a single point, which

*norris@rutgers.edu

Electronic supplementary material is available at <http://dx.doi.org/10.1098/rspa.2008.0076> or via <http://journals.royalsociety.org>.

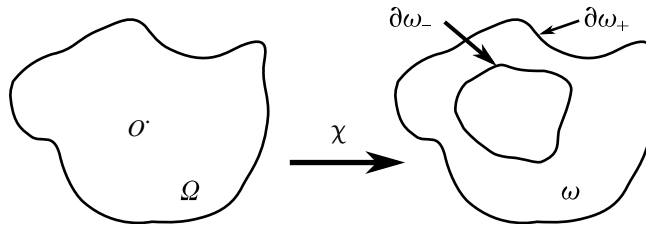


Figure 1. The undeformed simply connected region Ω is transformed by the mapping χ into the multiply connected cloak ω . Essentially, a single point O is transformed into a hole (the invisible region) surrounded by the cloak ω . The outer boundary $\partial\omega_+$ is coincident with $\partial\Omega_+$ ($=\partial\Omega$) and the inner boundary $\partial\omega_-$ is the image of the point O . Apart from O and $\partial\omega_-$ the mapping is everywhere one-to-one and differentiable.

is mapped into the cloak inner boundary (figure 1). The acoustic problem is for the infinitesimal pressure $p(\mathbf{x}, t)$ that satisfies the scalar wave equation in the surrounding fluid,

$$\nabla^2 p - \ddot{p} = 0. \quad (1.1)$$

The basic idea is to alter the cloak's acoustic properties (density and modulus) so that the modified wave equation in ω mimics the exterior equation (1.1) in the *entire* region Ω . This is achieved if the spatial mapping of the simply connected region Ω to the multiply connected cloak ω has the property that the modified equation in ω when expressed in Ω coordinates has exactly the form of (1.1) at every point in Ω .

The objective here is to answer the question: what type of material is required to realize these unusual properties that make an acoustic cloak? While cloaking cannot occur if the bulk modulus and density are simultaneously scalar quantities (see below), it is possible to obtain acoustical cloaks by assuming that the mass density is anisotropic (Chen & Chan 2007; Cummer & Schurig 2007; Cummer *et al.* 2008). A tensorial density is not ruled out on fundamental grounds (Milton *et al.* 2006) and in fact there is a strong physical basis for anisotropic inertia. For instance, Schoenberg & Sen (1983) showed that the inertia tensor in a medium comprising alternating fluid constituents is transversely isotropic (TI) with elements $\langle \rho \rangle$ in the direction normal to the layering, and $\langle \rho^{-1} \rangle^{-1}$ in the transverse direction, where $\langle \cdot \rangle$ is the spatial average. Anisotropic effective density can arise from other microstructures, as discussed by Mei *et al.* (2007) and Torrent & Sánchez-Dehesa (2008). The general context for anisotropic inertia is the Willis equations of elastodynamics (Milton & Willis 2007), which Milton *et al.* (2006) showed are the natural counterparts of the electromagnetic (EM) equations that remain invariant under spatial transformation. The acoustic cloaking has been demonstrated, theoretically at least, in both two and three dimensions: a spherically symmetric cloak was discussed by Chen & Chan (2007) and Cummer *et al.* (2008), while Cummer & Schurig (2007) described a two-dimensional cylindrically symmetric acoustic cloak. These papers use a linear transformation based on prior EM results in two dimensions (Schurig *et al.* 2006).

The cloaks based on anisotropic density in combination with the inviscid acoustic pressure constitutive relation (bulk modulus) will be called inertial cloaks (ICs). The fundamental mathematical identity behind the ICs is the

observation of Greenleaf *et al.* (2007) that the scalar wave equation is mapped into the following form in the deformed cloak region:

$$\frac{1}{\sqrt{|g|}} \frac{\partial}{\partial x_i} \left(\sqrt{|g|} g^{ij} \frac{\partial p}{\partial x_j} \right) - \ddot{p} = 0, \quad \mathbf{x} \in \omega. \quad (1.2)$$

Here $g = (g_{ij})$ is the Riemannian metric with $|g| = \det(g_{ij})$ and $(g^{ij}) = (g_{ij})^{-1}$. The reader familiar with differential geometry will recognize the first term in equation (1.2) as the Laplacian in curvilinear coordinates. Comparison of the transformed wave equation (1.2) with the IC wave equation provides explicit expressions for the IC density tensor and the bulk modulus (Greenleaf *et al.* 2008).

We will derive an identity equivalent to (1.2) in §2 using an alternative formulation adapted from the theory of finite elasticity. A close examination of the anisotropic density of the ICs shows that its volumetric integral, the total mass, must be infinite for perfect cloaking. This raises grave questions about the usefulness of the ICs. The rest of this paper provides a solution to this quandary. The main result is that the IC is a special case of a more general class of the acoustic cloaks, defined by anisotropic inertia combined with anisotropic stiffness. The latter is obtained through the use of the pentamode materials (PMs; Milton & Cherkaev 1995). In the same way that an ideal acoustic fluid can be defined as the limit of an isotropic elastic solid as the shear modulus tends to zero, there is a class of limiting anisotropic solids with five (hence penta) easy modes of deformation analogous to shear, and one non-trivial mode of stress and strain. The general cloak comprising PM and IC is called the PM-IC model. The additional degrees of freedom provided by the PM-IC allow us to avoid the infinite mass dilemma of the IC.

We begin in §2 with a new derivation of the IC model, and a discussion of the infinite mass dilemma. The PMs are introduced in §3 where it is shown that they display simple wave properties, such as an ellipsoidal slowness surface. The intimate connection between the PM and the acoustic cloaking follows from theorem 4.2 in §4. The properties of the generalized PM-IC model for cloaking are developed in §4 through the use of an example cloak that can be either pure IC or pure PM as a parameter is varied. Further examples are given in §5, with a concluding summary of the generalized acoustic cloaking theory in §6.

2. The IC

The transformation from Ω to ω is described by the point-wise deformation from $\mathbf{X} \in \Omega$ to $\mathbf{x} = \boldsymbol{\chi}(\mathbf{X}) \in \omega$. In the language of finite elasticity, \mathbf{X} describes a particle position in the Lagrangian or undeformed configuration and \mathbf{x} is particle location in the Eulerian or deformed physical state. The transformation or mapping defined by $\boldsymbol{\chi}$ is one-to-one and invertible except at the single point $\mathbf{X} = \mathbf{O}$ (figure 1). We use ∇ , $\nabla_{\mathbf{X}}$ and div , Div to indicate the gradient and divergence operators in \mathbf{x} and \mathbf{X} , respectively. The component form of $\text{div } \mathbf{A}$ is $\partial A_i / \partial x_i$ or $\partial A_{ij} / \partial x_i$ when \mathbf{A} is a vector or a second-order tensor-like quantity, respectively. The deformation gradient is defined as $\mathbf{F} = \nabla_{\mathbf{X}} \mathbf{x}$ with inverse $\mathbf{F}^{-1} = \nabla \mathbf{X}$, or in component form $F_{iI} = \partial x_i / \partial X_I$ and $F_{Ii}^{-1} = \partial X_I / \partial x_i$. The Jacobian of the deformation is $J = \det \mathbf{F} = |\mathbf{F}|$ or, in terms of volume elements in the two